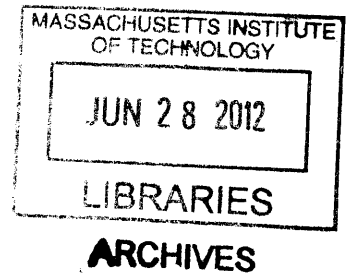# Adsorption at the Nanoparticle Interface for Increased Thermal Capacity in Solar Thermal Systems

by

Matthew W. Thoms

B.S., Mechanical Engineering (2010)

Tufts University

Submitted to the Department of Mechanical Engineering in

Partial Fulfillment of the Requirements for the

Degree of Master of Science in Mechanical Engineering

at the

Massachusetts Institute of Technology

June 2012

Signature of Author: ....

Department of Mechanical Engineering
May 23, 2012

Certified by: ....

Evelyn N. Wang
Associate Professor of Mechanical Engineering
Thesis Supervisor

Accepted by: ....

David E. Hardt
Chairman, Department Committee on Graduate Students

Adsorption at the Nanoparticle Interface for Increased Thermal Capacity in Solar Thermal Systems

by

Matthew W. Thoms

Submitted to the Department of Mechanical Engineering on May 23rd, 2012, in Partial Fulfillment of the Requirements for the Degree of Master of Science

Abstract

In concentrated solar power (CSP) systems, high temperature heat transfer fluids (HTFs) are responsible for collecting energy from the sun at the solar receiver and transporting it to the turbine where steam is produced and electricity is generated. Unfortunately, many high temperature HTFs have poor thermal properties that inhibit this process, including specific heat capacities which are half that of water. In an effort to enhance the effective heat capacity of these high temperature HTFs and thus increase the efficiency of the CSP systems, adsorption energy at the liquid-solid interface was investigated as a mechanism for increased thermal capacity.

Solid ceramic nanoparticles were dispersed in several molten salts at 1-2% by mass with diameters ranging from 5 nm to 15 nm to provide a significant available surface area for adsorption at the particle-molten salt interface. After successful nanofluid synthesis, differential scanning calorimetry (DSC) was used to measure anomalous deviations from the expected heat capacity and enthalpy of fusion values in the nanofluids. The variation in the sensible and latent heat values was determined to be dependent on the presence of sub-100 nm particles and attributed to a layer of salt that remains adsorbed to the surface of the nanoparticles after the bulk of the salt has melted. The adsorbed salt layer is expected to desorb at a higher temperature, providing an increased effective thermal capacity in the vicinity of this desorption temperature.

A thermal analysis technique utilizing DSC was proposed to approximate the thickness of the adsorbed layer at the liquid-solid interface, a value that has previously only been obtained using simulation or transmission electron microscopy. More specifically, the adsorbed layer of $LiNO_3$ on Al_2O_3 particles was determined to be 5.3-7.1 nm thick, similar to the 1-3 nm layers that have been observed in literature for simple, monatomic fluids. The results provide new insight into the nature of adsorption at the liquid-solid interface in more complex fluid and particle systems that can be harnessed for enhanced thermal capacity in HTFs.

Thesis Supervisor: Evelyn N. Wang

Title: Associate Professor, Mechanical Engineering

Acknowledgements

Contents

List of Figures

9

List of Tables

Chapter 1

1. Introduction

1.1   MOTIVATION

The annual global energy consumption has quadrupled from 100 exajoules to well over 400 exajoules [1], [2] over the past 50 years. It is expected to follow this trend as the global population continues to increase along with the energy requirements as more and more nations become developed. Furthermore, the vast majority of the energy generation processes release considerable amount of harmful chemicals (*e.g.*, CO_2, NO_x, and SO_x) resulting in severe environmental implications. The 2007 Intergovernmental Panel on Climate Change (IPCC) report, a study that was awarded the 2007 Nobel Peace Prize, concluded that the use of fossil fuels since the industrial revolution is responsible for the global increase in temperatures and the abnormally high concentrations of CO_2 in the atmosphere [3], [4]. As a result of these ever-increasing environmental concerns and the associated policy changes, there has been an unprecedented increase in the number of research efforts towards developing cleaner and renewable sources of energy.

One of the most promising technologies for providing the world with a sufficient supply of clean and renewable energy is solar power. The average solar flux reaching the surface of the earth is about 1367 W/m^2 after considering the reflectance of various atmospheric gases. This amounts to an estimated $1.8*10^{16}$ kWh of energy over the entire area of the United States [5], [6]. Comparing this to the annual United Stated consumption of about $2.9*10^{13}$ kWh (0.16% of the incoming energy) [7] clearly highlights the potential of the solar energy as the inevitable solution. However, low conversion efficiencies of around 20% [2] are preventing widespread adoption of solar power and advances in solar technology are required to make device operation more efficient and cost competitive with fossil fuel alternatives.

Devices for utilizing solar radiation come in two main flavors. Photovoltaic (PV) devices convert solar radiation directly into electrical energy by allowing photons to excite charge carriers in doped semiconducting materials. Although PV devices are expensive at about 25¢/kWh (compared to 3¢/kWh for most fossil fuel systems) and have low solar to electrical

conversion efficiencies of around 15% [2], the compact form factor of a PV system allows them to be installed in small, decentralized locations such as rooftops and feed electricity directly into the existing electrical grid infrastructure. In solar thermal devices, the thermal energy of the sun is harnessed directly by heating an appropriate heat transfer fluid (HTF). This heat can either be used directly for domestic hot water, industrial process heat, and other thermal applications or it can be used to drive a steam cycle and generate electricity. Concentrated solar power (CSP) plants use solar thermal energy for electricity production and are not as scalable as PV systems, often requiring a larger installation. Compared to PV systems, CSP has a slightly higher solar to electrical conversion efficiency of about 20% and is much more economical at around 6¢/kWh [8]. While kilowatt scale electricity production can be handled with PV panels, electricity generation from CSP is more appropriate for megawatt scale units in order to replace the conventional fossil fuel based power plants [9].

In a CSP plant, an array of mirrors is used to focus light on a heat transfer fluid that is used to create steam which is then utilized in a heat-engine cycle (often a Rankine cycle [9]) to generate electricity. Two popular designs are the parabolic trough design where a pipe carrying the HTF lies at the focal point of an elongated parabolic mirror and the power tower design where a field of heliostats focuses light on a vat containing the HTF atop a tall tower as seen in Figure 1.
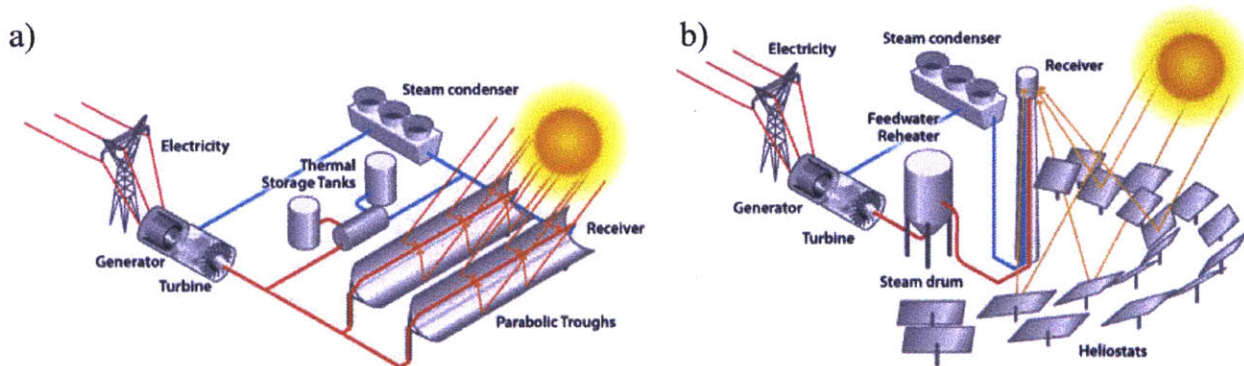
Figure 1. (a) Parabolic trough design and (b) power tower design for CSP plant [10].

In both designs, a large factor in the efficiency of CSP is the properties of the HTF when operating at extremely high temperatures, often upwards of 400°C [11]. Given that the thermodynamic efficiency of a CSP plant is directly related to the highest achievable temperature, it is advantageous to run the plant at as high of a temperature that can be safely

14

attained. In many cases, the HTF is the limiting factor in reaching these high temperatures [11]. Furthermore, the HTFs that are stable at these high temperatures, namely synthetic oils and salt eutectics, suffer from poor thermal properties in comparison to water.

A simple schematic of a CSP cycle is shown in Figure 2. The solid line on the right side of the cycle uses water as a working fluid and operates as a standard Rankine cycle with a heat exchanger in place of a boiler. The dashed line uses a high temperature HTF to achieve a higher temperature at reasonable pressures exiting the solar receiver than are possible if water were used. In the heat exchanger, the HTF converts the incoming water into superheated steam for a high thermodynamic efficiency. Superheating the steam directly in the solar receiver is often prohibitively difficult due to the high pressures produced and the fragile nature of the receiver [12]. Thus, a liquid loop with a contained high temperature HTF is often favorable. This thesis focuses on HTFs used in this application.
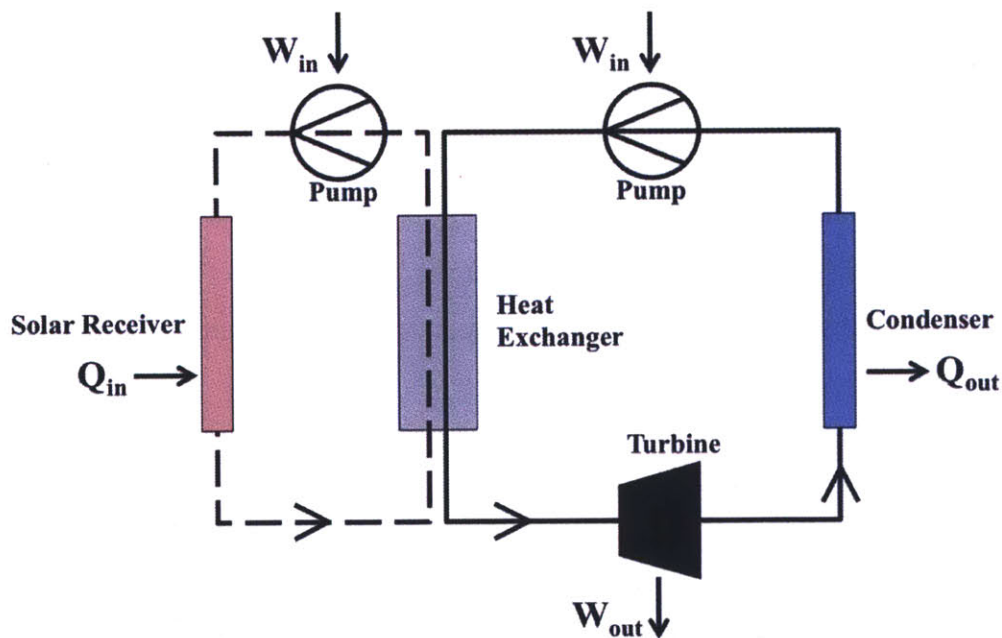
Figure 2. A simple diagram of a CSP cycle. A high temperature HTF is used on the receiver side (dashed) while water is used as the working fluid for the Rankine cycle (solid).

The objective of this thesis is to assess the possibility of increasing the effective heat capacity of high temperature molten salt heat transfer fluids by utilizing the liquid-solid adsorption energy at the surface of ceramic nanoparticles. By experimentally investigating the nature of adsorption

15

at the liquid-solid interface, nanofluids with an extremely large particle surface area available for adsorption can potentially be engineered to harness this phenomenon for thermal benefits. The nascent concept of utilizing the thermal energy of liquid-solid adsorption is largely unexplored both in theory and application. This thesis provides the data and analysis necessary to probe the potential of this fundamental mechanism in the context of solar heat transfer fluids. Once well understood, the benefits of liquid-solid adsorption can be harnessed in a variety of fluid-substrate combinations for an abundance of thermal fluid applications.

1.2   BACKGROUND

1.2.1   High Temperature Solar Heat Transfer Fluids

To advance CSP efficiency, high temperature HTFs play a large role [11]. In addition to optical properties that allow for the solar HTF to absorb as much incident sunlight as possible, the thermal properties of the HTF are also a crucial factor. An ideal solar HTF is required to have a large liquid temperature range extending to high temperatures at reasonable operating pressures. This prevents the HTF from freezing in the event of low solar irradiation due to sudden cloud cover or other events. While power tower designs often include quick drainage systems as a defense against freezing, parabolic trough plants largely lack this feature and the solar receiver equipment can be damaged by freezing of the HTF [3], [11]. Further, the maximum operating temperature of the plant is required to be well below the temperature at which the HTF decomposes.

The Carnot efficiency of the steam cycle used to produce electricity, defined in Equation 1, favors a low cold temperature and a high hot temperature for maximum efficiency.

$$\eta_{carnot} = 1 - \frac{T_{hot}}{T_{cold}} \tag{1}$$

The cold temperature, T_{cold}, is mostly dictated by ambient conditions providing little room for improvements in the overall temperature range. The high temperature, T_{hot}, however, is the temperature of the superheated steam after it has been heated by a heat exchanger with the HTF. Thus, the higher the temperature at which the HTF can safely operate, the more efficient the steam cycle will run. While this temperature can be limited by the material constraints of the

16

system components, the decomposition temperature of the HTF is often the limiting factor [12], [13].

Although a number of candidates are well suited to achieve higher temperatures and larger operating ranges than water, other thermal properties suffer as a result. Namely, the specific heat capacity, the amount of energy needed to raise one gram of substance by one degree Celsius, is drastically reduced in the candidate HTFs as seen in Table 1. Heat capacity is a crucial metric for evaluating the efficacy of a solar HTF as it indicates how much thermal energy can be transported from the solar collectors to the heat exchanger where steam is produced. With a high heat capacity HTF, either the size of the plant's solar collectors can be reduced at the same energy output, reducing the material cost of the plant, or more steam and thus more electricity can be extracted from the same amount of HTF [5], [14], [15]. In both cases, a HTF with a larger heat capacity will ultimately reduce the cost per kWh of CSP plants.

While water may seem like a great option for a solar HTF due to its excellent heat capacity value, water proves to be prohibitively difficult and expensive to keep in liquid form above 100°C due to its high vapor pressure at these temperatures [12]. A number of alternate HTFs have been proposed and even employed in the CSP community in order to sustain high operating temperatures without decomposition or exhibiting an excessive vapor pressure. One popular option is Therminol VP-1, a commercial synthetic oil that is a eutectic mixture of Diphenyl-oxide and Biphenyl [16]. VP-1 is liquid and stable from 13-400°C, an acceptable operating range for CSP applications [11]. In an effort to achieve even higher operating temperatures for increased thermodynamic efficiency, the CSP community has turned to various salt eutectics. One commercial solar salt, Hitec HTS, is a KNO_3-$NaNO_3$-$NaNO_2$ eutectic with a liquid range of 120-500°C [11]. While the maximum operating temperature is higher than the synthetic oils, the raised melting temperature can still be problematic for CSP plant operation. Room temperature ionic liquids (RTIL) are a class of salts composed of an organic cation and inorganic anion [17]. Although not yet commercialized for CSP applications, RTILs promise stable temperatures in excess of 450°C while maintaining a freezing point below room temperature [11]. Ongoing research looks to further improve this temperature window, allowing RTILs to remain stable at even higher temperatures.

Table 1. Heat capacities of solar heat transfer fluid candidates [11].

Heat Transfer Fluid	Specific Heat Capacity (J/g°C)	Operating Temperature (°C)
Water	4.18	1 – 100
Therminol VP-1	2.32	13 – 400
Hitec XL	1.45	120 – 500
Ionic Liquid (omimBF$_4$)	2.50	20 – 450

1.2.2   Reports of Increased Heat Capacity in Heat Transfer Fluids

In one of the most popular efforts to increase the effective heat capacity of HTFs, numerous studies have suggested the use of small particles of phase change material (PCM) [18-25]. The purpose of a PCM is to undergo a first order phase transition from a solid to liquid at a temperature that is within the useful operating temperature range of the HTF. The enthalpy of fusion of the PCM acts as a mechanism for absorbing thermal energy and the PCM/liquid slurry consequently has a higher effective heat capacity than the pure liquid. Enthalpy of fusion values for PCMs are on the order of 100 J/g and at 10% weight concentration in the fluid mixture will contribute 10 J/g (2 J/g°C over a 5°C PCM melting region) to the thermal capacity of the fluid [23]. Typically, paraffin waxes or fatty acids are used as a PCM, often as micro- or nano-scale particles encapsulated in a polymer shell to prevent agglomeration [23] as seen in Figure 3.
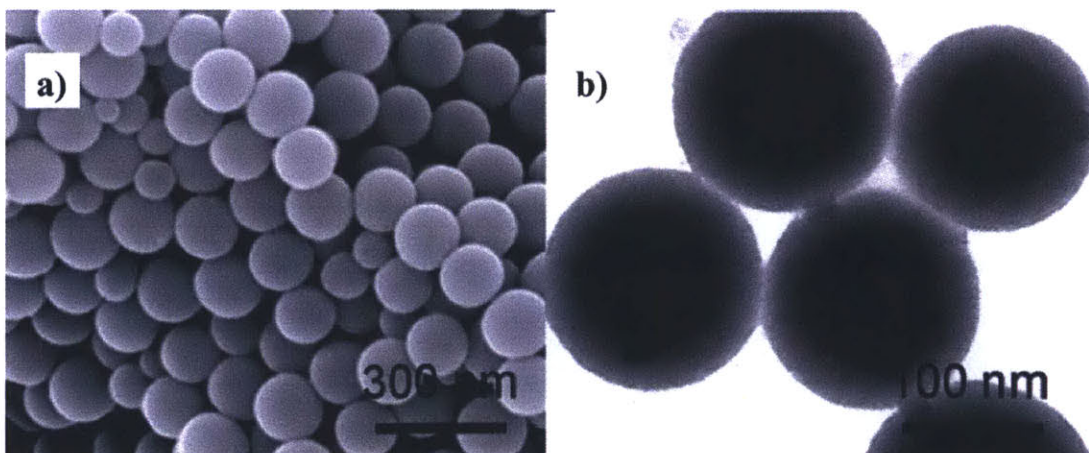
Figure 3. (a) SEM and (b) TEM images of polystyrene encapsulated paraffin particles [26].

18

While numerical simulations have shown increased Nusselt numbers (and thus increased convective heat transfer) in slurries of PCM and a common HTF [25], a handful of logistical issues arise when using PCM slurries in practice. Namely, encapsulated PCM do not perform well after multiple melt/freeze cycles. The encapsulation shells are prone to burst due to thermal expansion of the contained PCM or can be crushed when passing through a pump [23]. Additionally, the high PCM particle mass concentrations (up to 30%) in the slurries causes a substantial increase in the fluid viscosity and likewise a large pressure drop across the channel of interest [25].

More importantly for CSP development, relatively little work has been done on PCM slurries for high temperature applications. This is likely due to the difficulty of finding suitable PCMs for high temperature as well as appropriate encapsulation materials. Studies that investigate high temperature PCM candidates are more often for applications where the PCM is a large stationary mass, rather than encapsulated and introduced into the HTF [3], [27]. This arrangement introduces an additional thermal resistance as a heat exchanger must be implemented between the HTF and the PCM. Clearly, the conventional idea of PCM and PCM slurries has many challenges for high temperature CSP applications. Thus, the salient question remains: how can the effective heat capacity of high temperature HTFs be increased while avoiding the issues associated with PCMs?

Early reports suggest that such a feat is possible, although the mechanism for increased heat capacity is not fully understood. Recent studies have reported experimental results of high temperature molten salt eutectics with heat capacities enhanced by between 5% and 100% [3], [15], [28-32]. These salts are all carbonate eutectics, often Li_2CO_3-K_2CO_3 (62:38 molar ratio), with a melting point of 488°C. In the most promising experiments, the carbonate salt was mixed with 1.5% by weight SiO_2 nanoparticles with ~10 nm diameter to yield a 100% increase in the salt's liquid heat capacity [3]. In similar studies, other ceramic nanoparticles and carbon nanotubes were used in small weight fractions to increase the liquid heat capacity of the carbonate eutectic salt.

In literature, these anomalous enhancements are attributed to several concurrent nano-scale phenomena illustrated in Figure 4. Shin, *et al.* reported that nanoparticles have been reported to exhibit up to a 25% increase in heat capacity from their bulk value shown in Mode I of Figure 4 [29]. Upon further examination, the enhancement in nanoparticle heat capacity is not a possible

contribution to the increased heat capacity of the nanofluid. Given that the heat capacity of bulk SiO_2 is 1.07 J/g°C, a 25% increase in this value yields a heat capacity of 1.34 J/g°C for the nanoparticles of interest. Given that the liquid phase of the carbonate eutectic has a heat capacity of 1.619 J/g°C [3], the addition of any fraction of SiO_2 will decrease the effective heat capacity of the salt.

Other possible mechanisms rely on the high available surface area of the nanoparticles when suspended in the molten salt. One proposed explanation asserts that the particle-liquid interface has an abnormally high interfacial resistance, illustrated in Mode II of Figure 4 [29]. It is hypothesized that the large interfacial resistance acts as a mechanism for thermal energy storage; however, this theory has minimal support in literature, both experimentally and theoretically. Finally, the presence of a dense, semi-solid layer of liquid particles on the surface of the nanoparticles is believed to contribute to the increase in heat capacity of the nanofluid as shown in Mode III of Figure 4 [29]. The benefit is attributed to the thermal properties of the adsorbed liquid layer; yet, given that the heat capacity of the solid salt is less than that of the liquid salt, there is little reason to believe that a semi-solid state of the salt would possess a higher heat capacity than either of the phases. While a number of potential explanations for the experimental results have been proposed, it is clear that a fundamental and comprehensive theory for the behavior of nanoparticles in solution is needed. With an improved understanding of the nano-scale phenomenon, the solutions and nanoparticles can be better optimized for thermal energy storage applications.
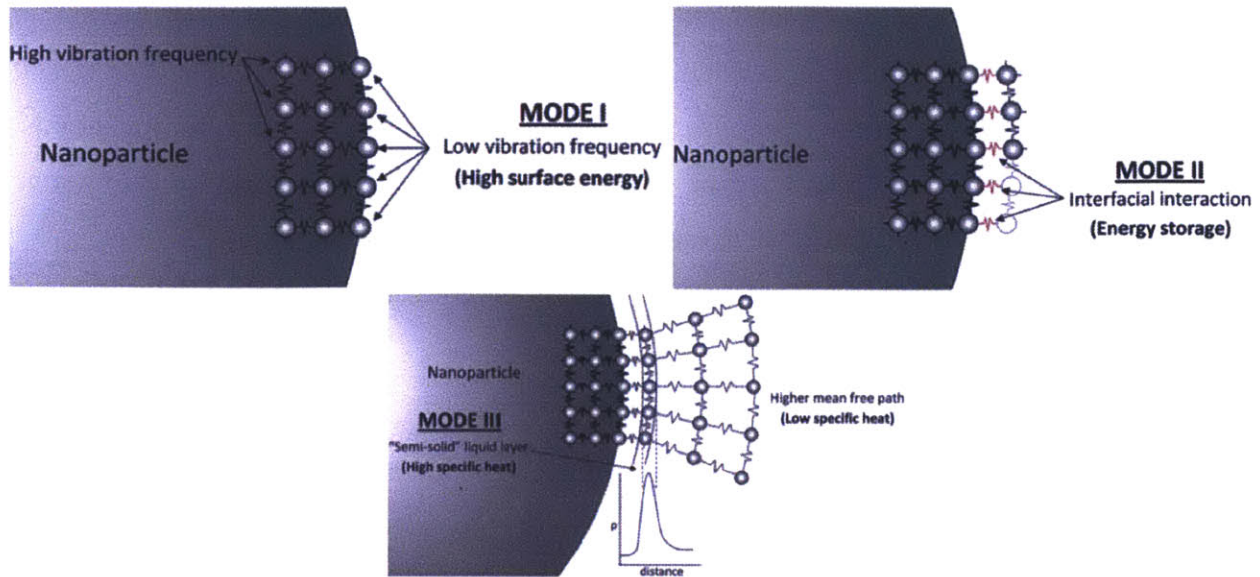
Figure 4. Proposed mechanisms for increased specific heat of eutectic salt nanofluids [29].

1.2.3   Reports of Adsorption at the Liquid/Solid Interface

In nanoparticle solutions, the behavior of the fluid in the close vicinity of the particle interface is very important. Due to the small size of the particles, the exposed surface area per unit volume of nanoparticles is drastically higher than that of micro and macro sized particles. The available surface area scales with r^{-1} so that an order of magnitude difference in particle size (*e.g.,* for 10 nm particles compared to 100 nm particles) also leads to an order of magnitude difference in available surface area for the same mass fraction of particles. In most particle mixtures (with micro scale or larger particles), interactions that occur within only a few nanometers of the liquid/particle interface are negligible compared to the mass of the fluid and the particles themselves. However, when the particle size is sufficiently small, the nanometer-thin region on the surface of the particles comprises a fraction of the mixture that is on the order of the particles and the bulk liquid. In this case, short scale interactions such as Van der Waals forces and the dipole-dipole interactions can no longer be neglected and may drastically alter the behavior of the fluid as compared to bulk properties.

In order to understand the properties of such mixtures, it is first important to investigate the behavior of liquid molecules at a liquid-solid interface. While this area has long been of interest for tribologists and fundamental scientists alike, it has only been closely studied since the mid-

1980s due to limitations in scientific capabilities [33], [34]. Density-functional theory has been used to quantify the interactions of solid and liquid substances at the interface [34]. As seen in Figure 5, the analytical approach predicts an intermediate phase over a few atomic distances at the interface with a density much larger than the bulk liquid. While this system is for monatomic fluids, the results suggest that liquid behaves differently when within reach of short-range adsorption forces and may be applicable to more complex HTFs.
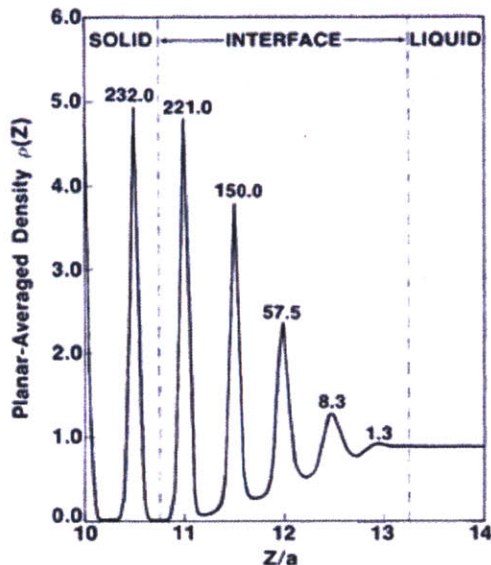
Figure 5. Density at a liquid-solid interface as predicted with density-functional theory [34].

More advanced molecular dynamics (MD) simulations studied liquid calcium silicate at the surface of solid alumina and silicon nitride substrates [35], [36]. In these simulations, the first several atomic distances from the substrate exhibited a similar ordering behavior to the density-functional theory approximation. Additional MD simulations suggest a stronger ordering effect in liquids that wet the substrate of interest when compared to those that are non-wetting [5]. This relationship is feasible as it is expected that both wettability and the thickness of adsorbed layer are a reflection of the bond strength between the liquid and solid molecules.

22
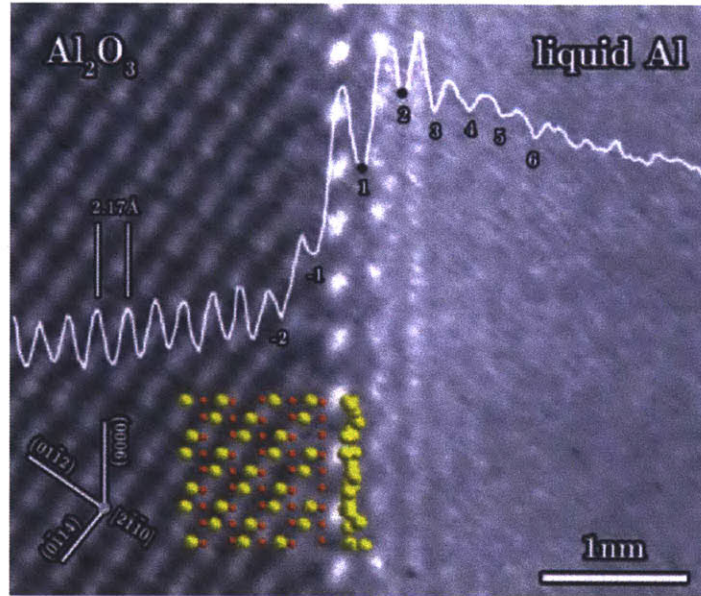
Figure 6. TEM image of solid alumina and liquid aluminum interface depicting an ordered liquid layer [37].

The ordering behavior of fluids at a solid interface has also been imaged using transmission electron microscopy (TEM) [13], [37]. Imaging this layer requires the liquid to have a lower vapor pressure than the ultrahigh vacuum pressure of the TEM. This limits the experiments to liquid metals at high temperatures or requires a TEM environmental chamber to protect the liquid from evaporation under the high vacuum. Additionally, the ordered interfacial layer is so thin (about 1 nm) that image-processing techniques are necessary to confirm that any apparent ordering is not due to imaging artifacts from the TEM [37]. As seen in Figure 6, liquid aluminum exhibits an approximately one-nanometer thick compressed layer at the interface with solid alumina, similar to what was predicted using MD simulations. The liquid ordering effect seen in TEM images has also been confirmed by using nuclear magnetic resonance (NMR) to experimentally determine the thickness of the interfacial layer [38].

1.2.4 Thermal Properties of Interfacial Liquid Layer

When attempting to utilize the ordering effect at the liquid solid interface for CSP applications, the thermal properties of the interfacial layer are crucial. One of the most prevalent topics in literature relating to thermal properties and liquid-solid interfaces is that of deviations in the melting temperature of liquid from bulk values. While the Gibbs-Thomson equation can be

used to predict adjustments in the melting temperature of liquids in macro-scale pores due to surface tension and capillary forces, the understanding of melting temperature of liquids within nano-scale pores and adsorbed to solid substrates is much less developed. Due to the difficulty with experimental measurements at the nano-scale, much of the research on this subject is computational in nature. In Monte Carlo and MD simulations, adsorbed layers on a solid substrate have been shown to melt at a higher, similar, or lower temperature based on whether the attraction of the adsorbate to the substrate is stronger, comparable, or weaker than the attraction to the bulk liquid, respectively [14], [39]. Radhakrishnan, *et al.* have made efforts to quantify the relative attraction of an adsorbed layer to the substrate versus the bulk liquid [14]. A relative parameter to gauge the strength of interaction, α, is used where $\alpha > 1$ denotes a strong attraction to the substrate and a higher local melting temperature, $\alpha \approx 1$ denotes a comparable attraction between the substrate and the bulk liquid for a similar melting temperature to bulk liquid, and $\alpha < 1$ denotes a weaker attraction to the substrate than the bulk material and thus a lower local melting temperature. In Figure 7, several simple adsorbates were characterized with respect to silica and graphite substrates. The use of MD simulations to determine the interaction parameter limits the phase diagram to relatively simple fluids that can be difficult and impractical to test experimentally. Nonetheless, the adsorbed interfacial layer shows potential for enhanced thermal properties over the bulk liquid.

Silica   Graphite

α

2 — Ar N_2

     CH_4

2 — Ar CO_2 Kr

   CH_4 Kr   Xe

   N_2 CO_2 CCl_4

     HI HCl

1 — HCl HI Xe $C_6H_5NO_2$

  $C_6H_5NO_2$ CCl_4

  NH_3 NH_3

     H_2O

  H_2O

0
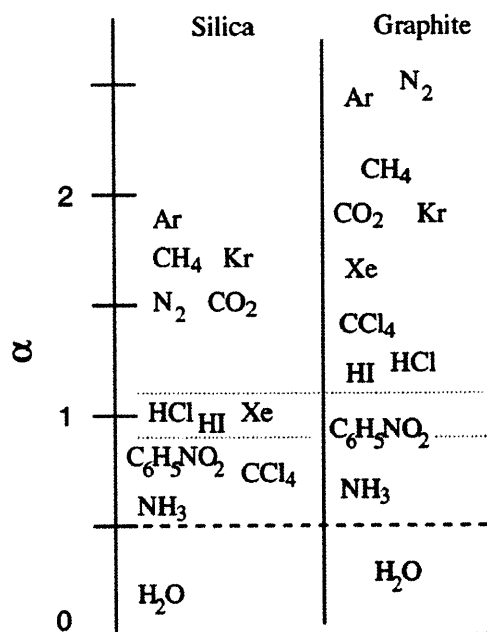
Figure 7. Expected relative change in melting temperature of interfacial layer for various adsorbates with silica or graphite substrate obtained by molecular dynamics simulations [14].

Melting point manipulation has been studied experimentally in highly porous substrates such as controlled pore glass (CPG), Vycor, and silicon nitride to allow for a high surface area to volume ratio of the substrate, similar to the effect created by using a nanoparticle mixture [40-42]. By using differential scanning calorimetry and dielectric relaxation spectroscopy, the melting temperatures of the components of the substrate/adsorbate mixture can be measured. In these studies, a decrease in melting temperature was measured for a fraction of In, CCl_4, and CCl_4-C_6H_5Br mixtures confined in the nanoporous substrate. These results are indicative of a weak interaction between the adsorbate and the porous substrate. While this behavior may be beneficial for some applications, increasing the thermal capacity of HTFs for CSP applications require an increased melting temperature of the adsorbed layer, as will be discussed shortly.

Although there is strong evidence, both experimentally and through simulations, that an adsorbed layer at the liquid-solid interface does exist and has unique thermal properties, little work has been done to explore its utility in heat transfer fluids for CSP and other thermal management applications. One area that has been explored is the role of the adsorbed layer in increasing the thermal conductivity of nanofluid mixtures. While much of the excitement from initial reports of anomalously high thermal conductivities in nanofluids has been disproven by

using the Hashin and Shtrikman effective medium theory [43], early reports investigated the role that the adsorbed layer at the nanoparticle surface may have in enhanced thermal conductivity [5], [44]. However, MD simulations indicate that the adsorbed interfacial layer (about 1 nm thick) has no effect on thermal transport properties for simple, monatomic liquids [5]. The reports mention the possibility that more complex liquids will have an adsorbed layer thicker than 1 nm and a different impact on thermal transport within the nanofluid. Further, while the thermal transport properties of the nanofluid remain largely unaffected, it is possible that the thermal storage properties are distinct from the pure fluid, as has been seen in the studies that manipulated the adsorbate melting point within nanopores.

1.3   THESIS OBJECTIVES AND OUTLINE

While concentrated solar power has significant potential to provide clean and renewable electricity generation, the poor thermal properties of high temperature heat transfer fluids create a significant bottleneck for increases in plant efficiencies. Previous attempts at using phase change materials to increase effective heat capacity in fluids have been shown to cause many operational complications and are not yet suitable for high temperature applications. A more robust alternative is to avoid the need for a phase change material by utilizing the energy of adsorption on the surface of solid nanoparticles for thermal energy storage. While few studies have attempted this nanofluid mixture experimentally, numerous studies report that an increase in melting temperature of an adsorbed layer compared to bulk values is possible, a phenomenon that can be harnessed for an increase in the thermal capacity of high temperature solar nanofluids.

By adding a small mass fraction of solid nanoparticles to a high temperature solar HTF, it is anticipated that the measured heat capacity of the nanofluid can increase due to the adsorption energy at the liquid-solid interface of the nanoparticle, provided that the liquid-solid attraction is sufficiently strong. The objective of this thesis is to experimentally confirm the effect of the liquid-solid adsorption energy on the thermal capacity of high temperature HTFs. The experimentation focuses on differential scanning calorimetry, while x-ray diffraction and thermogravimetric analysis are also utilized. Through this research, key parameters have be identified to optimize the effect and tailor the enhanced temperature range for a variety of thermal fluid applications. With experimental results and modeling efforts, the fundamental

mechanism behind any increases in thermal capacity can begin to be understood. The findings of this work are relevant to potentially increasing the efficiency of CSP plants by creating more effective high temperature HTFs while furthering the understanding of nanoscale heat and mass transfer that may be applicable to a number of thermal systems. The structure of this thesis is outlined below:

In Chapter 1, the necessity for more efficient solar power was discussed as well as previous efforts at increasing the thermal capacity of heat transfer fluids. Upon reviewing fundamental studies of adsorption at the liquid-solid interface and melting point manipulation at the nanoscale, a hypothesis is presented for enhancing the thermal capacity of high temperature heat transfer fluids by utilizing the adsorption energy on the surface of nanoparticles.

In Chapter 2, approximations for the thermal capacity of nanofluid mixtures are presented using current models and models that have been modified to accommodate adsorption effects. Key parameters are identified for maximizing the utility of adsorption at the liquid-solid interface.

In Chapter 3, the experimental methodology for the studies is explained. This includes the justification for the selection of adsorbate and adsorbent as well as a description of the relevant experimental equipment.

In Chapter 4, experimental results are presented for several adsorbate and adsorbent combinations. The discussion includes details of successful sample preparation, the intricacies involved with experiments using molten salt heat transfer fluids, and analysis of the reliability of experimental results.

In Chapter 5, the data acquired in Chapter 4 is analyzed in more detail. Trends in the data are explained as they relate to the adsorption hypothesis and the consistency with the expected results is discussed.

In Chapter 6, the experiments and analysis presented in the thesis are summarized. Modifications to the original hypothesis as well as suggestions for future experiments are discussed.

2. Predicting Enhanced Heat Capacity of Nanoparticle Mixtures

In order to understand the relative significance of the variables in a nanoparticle mixture, it is crucial to make approximations of the expected thermal enhancements by modeling the behavior of the mixture. The information obtained from these efforts will enable the nanofluid that is used in experiments to demonstrate the anticipated enhancement in heat capacity.

2.1 INCREASING THERMAL CAPACITY WITH ADSORPTION ENERGY

Before estimating the increased thermal capacity of nanofluids, it is essential to understand the nature of the enhancement. In light of the previous research presented in Chapter 1, there appears to be a mechanism for increasing the effective heat capacity of high temperature HTFs for CSP applications. When a small fraction of solid nanoparticles are added to a HTF, a thin layer of HTF is adsorbed to the surface of the particles [5]. The scale of this adsorbed layer is reported to be in the single nanometer range; however, the mass fraction of the adsorbed layer may be large for sufficiently small particle sizes due to the high surface area to volume ratio of nanoparticles. If a fluid and particle combination is chosen such that the fluid is more strongly attracted to the particle than it is to the bulk fluid, a local increase in melting temperature is expected for the adsorbed liquid layer. In this instance, a thin adsorbed layer may remain on the surface of the nanoparticles after the bulk of the liquid has melted. If the temperature continues to increase past the bulk melting temperature, the adsorbed layer is expected to desorb (or melt) while the rest of the HTF is in a liquid phase. The energy of desorption should behave similar to an enthalpy of fusion term and will increase the effective thermal capacity of the HTF over the liquid temperature range. While this value is often measured as a fluid's specific heat capacity, the actual mechanism in this case is a combination of sensible heat of the bulk fluid and the energy of desorption at the particle interface. Thus, the term "thermal capacity" is more appropriate than the common "heat capacity" terminology.

Given this nanoparticle mixture, the current literature suggests that one of two scenarios is likely to occur for an increased thermal capacity. The first case, as demonstrated in Figure 8, mirrors the results of the experiments that observed an anomalous increase in heat capacity of carbonate salt eutectics with ceramic nanoparticles. Once the bulk of the liquid melts, a compressed liquid layer (red) remains adsorbed to the surface of the nanoparticle (blue). As the temperature is increased, the adsorbed layer will slowly desorb with each atomic adsorbed layer requiring additional energy to desorb until the liquid has been entirely desorbed from the nanoparticle. The heat capacity values of the nanofluid (blue) will differ from the pure fluid (black) by having a decrease in latent heat from the adsorbed layer that has yet to melt while experiencing an increase in heat capacity over a finite temperature range. The decrease in latent heat can be seen in the smaller peak of the nanofluid on the left side of Figure 8. The increase in heat capacity occurs while the bulk of the fluid is in a liquid phase and the adsorbed layer is gradually desorbing as the temperature rises. Once the adsorbed layer has completely desorbed from the particle, the heat capacity will have the about the same value as the pure liquid, with a small adjustment for the heat capacity of the nanoparticles that is expected to be negligible for small mass fractions (~1%).
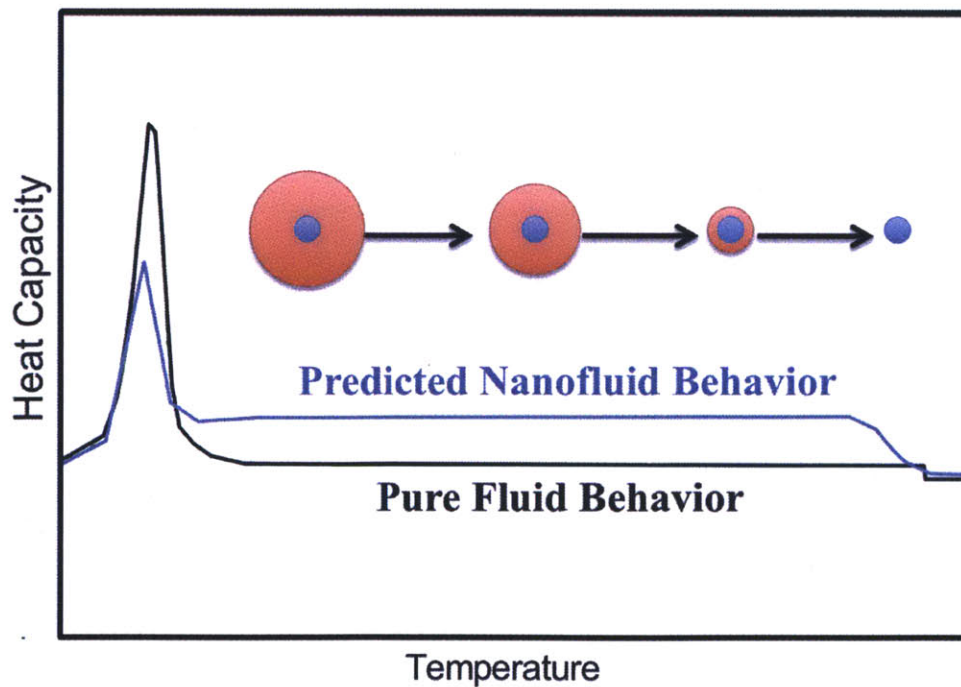
Figure 8. Schematic representation of predicted thermal behavior of adsorbed layer in nanofluid based on behavior reported in high temperature carbonate eutectic studies.

29

If the adsorbed layer in the nanofluid instead has a single increased melting temperature as the nanoporous substrate studies suggest, the thermal behavior of the nanofluid will differ from the previous case. The difference in heat capacity values as temperature increases is illustrated in Figure 9. In this scenario, the nanofluid (blue) will exhibit a decrease in latent heat compared to the pure substance (black) as the adsorbed layer remains in a solid-like compressed phase due to the strong attraction to the nanoparticle and has yet to undergo a change of phase, similar to the previous case. Since the nanoporous substrate studies report a single increased melting temperature of the adsorbed layer and not a layer-by-layer desorption, the adsorbed layer will remain adsorbed until the desorption temperature is reached. Before this temperature is reached, the nanofluid will have a lower liquid heat capacity than the pure substance. This is a result of the high mass fraction of adsorbate (red) in the nanoparticle mixture. The adsorbed layer is expected to be in a compressed, solid-like state [5] and thus is expected to have a similar sensible heat capacity to the solid phase of the adsorbate, which in many cases is less than that of the liquid phase [45]. Once the modified melting temperature of the adsorbed layer is reached, a small desorption peak, similar to an enthalpy of fusion term, will be seen as the adsorbed layer completely desorbs from the surface of the nanoparticles. After this point, the nanofluid will return to the heat capacity value that results from a mixing rule of the fluid and the nanoparticles that is nearly identical to the heat capacity of the fluid for small particle fractions.
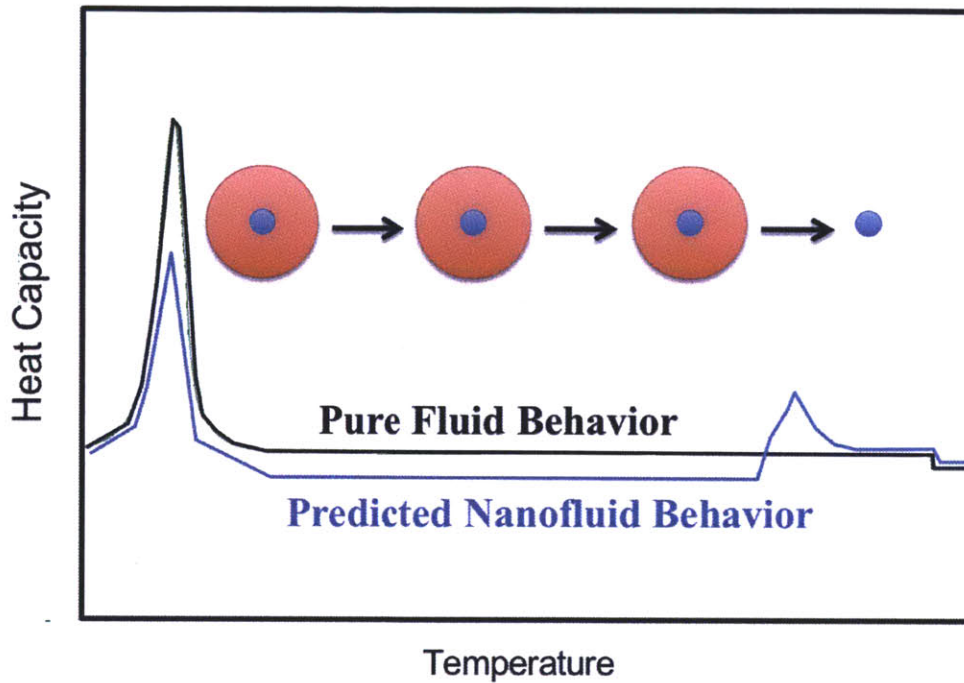
Figure 9. Schematic representation of predicted thermal behavior of adsorbed layer in nanofluid based on behavior reported in nanoporous substrate studies.

While there is evidence in literature to suggest that either of these scenarios is possible, one must be chosen for the purpose of approximating significant experimental parameters of the nanofluid. Although the two possible behaviors may exhibit slight differences in thermal properties, the important experimental variables are expected to be the same order of magnitude, placing less significance on which scenario is used for preliminary modeling. The first, layer-by-layer desorption scenario is used in the following sections for basic modeling due to its prevalence in literature with applications for high temperature HTFs for CSP plants [3], [15], [28], [29], [31], [32].

2.2 MODELING HEAT CAPACITY ENHANCEMENT

In traditional mixing theory, a simple mixing rule is used to predict the thermal properties of a two-component mixture. The rule for heat capacity, C_p, of a particle and liquid mixture can be seen in Equation 2. In this equation, ρ is density and ϕ is the mass fraction of particles as defined in Equation 3 where m is mass.

31

$$C_{p,Mixture} = \frac{\phi(\rho C_p)_{Particle} + (1-\phi)(\rho C_p)_{Fluid}}{\phi \rho_{Particle} + (1-\phi)\rho_{Fluid}} \tag{2}$$

$$\phi = \frac{m_{Particle}}{m_{Particle} + m_{Fluid}} \tag{3}$$

While this approach for determining heat capacity of a mixture is very common, even for nanoparticle mixtures [1], it is possible that this rule is inadequate in describing the true thermal capacity of a nanofluid. More specifically, the traditional mixing rule does not account for any thermal effects of adsorption at the surface of the nanoparticles. This effect may be negligible for particles with diameters on the order of 100 nm and larger, yet particles with diameters on the order of 10 nm have a high enough surface to volume ratio that the mass fraction of the adsorbed layer is significant [3].

In the instance where the nanoparticles are of this scale, a new approximation is necessary to quantify both the sensible heat of the fluid as well as the adsorption energy of the interfacial layer. First, a new term, γ, is introduced to quantify the mass fraction of the adsorbed layer and is defined in Equation 4. The mixing rule is now modified to balance the effective heat capacities of the three components of the nanofluid: the bulk fluid, the nanoparticle, and the adsorbed interfacial layer. The modified equation for effective heat capacity is seen in Equation 5.

$$\gamma = \frac{m_{Adsorbed}}{m_{Particle} + m_{Fluid} + m_{Adsorbed}} \tag{4}$$

$$C_{p,Mixture} = \frac{\phi(\rho C_p)_{Particle} + (1-\phi-\gamma)(\rho C_p)_{Fluid} + \gamma(\rho \frac{\Delta h_{Adsorption}}{\Delta T})_{Adsorbed}}{\phi \rho_{Particle} + (1-\phi-\gamma)\rho_{Fluid} + \gamma \rho_{Adsorbed}} \tag{5}$$

The modified mixing rule presents several new variables related to the quantification of the effective thermal capacity of the adsorbed layer. It should be noted that this modified mixing rule approximation for heat capacity assumes that the adsorbed layer will behave as described in the first scenario in this chapter, where the adsorbed layer slowly desorbs over a finite temperature range before completely desorbing. This temperature desorption range is the ΔT term in Equation

5. The term $\Delta h_{Adsorption}$ quantifies the enthalpy associated with the phase transition of the adsorbate from a compressed, semi-solid layer to a liquid phase. While it is possible that this desorption enthalpy may be calculated from molecular interaction theory for simple fluids, more complex fluids require that the value be measured experimentally. Measurements of enthalpy of desorption at the liquid-solid interface are inherently difficult to perform due to the nanometer scale of the phenomenon and is best quantified with a differential scanning calorimeter, although often with poor accuracy. If a calorimeter that measures heat flux at the nano-scale could be used, the enthalpy of desorption of an adsorbed layer at the liquid-solid interface could be accurately determined.

In order for this heat capacity approximation to yield useful information about key experimental parameters, a number of assumptions and simplifications are made. The mass fraction of the adsorbed layer, γ, is unknown and is estimated. However, since the nanoparticle size, concentration, and thus the available surface area are known, the mass fraction of adsorbate is related to the thickness of the adsorbed layer, a value that has been reported in literature [5].

The density, ρ, of the adsorbed layer is another unknown. The phase is expected to be a semi-solid state, but experimental evidence for density values is scarce. Based on reports of molecular dynamics and density functional theory at the liquid solid interface [13], [34], the density of the adsorbed layer is approximated as that of the solid phase of the adsorbate.

The effective heat capacity term for the adsorbed layer must also be approximated. In experimental reports of enhanced heat capacity in carbonate eutectic nanofluids, an increase in heat capacity is measured over approximately 50°C [3], [28], [29]. For the sake of this analysis, the desorption temperature range, ΔT, is assumed to be 50°C as well. Finally, the enthalpy of adsorption, $\Delta h_{Adsorption}$, remains unknown and is not easily obtained experimentally or even in simulations for more complex fluids. As an approximation, the enthalpy of fusion of the adsorbate is used instead. Since the particle-adsorbate attraction is expected to be stronger than the solid adsorbate-adsorbate bond, a requirement for the adsorbed layer to exist in a liquid adsorbate environment, any enhancement in heat capacity that is predicted by using the enthalpy of fusion approximation will in actuality underestimate the influence of the adsorbed layer.
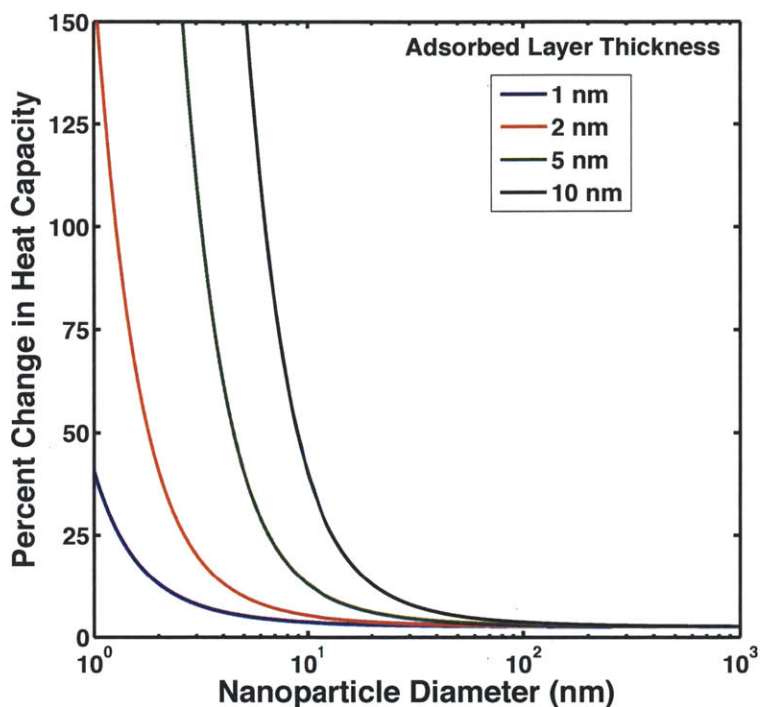
Figure 10. Predicted changes in heat capacity of LiNO$_3$ with 1% Al$_2$O$_3$ nanoparticles based on a modified mixing rule in Equation 5.

As will be described in Chapter 5, LiNO$_3$ with 1% by mass Al$_2$O$_3$ nanoparticles proved to be one of the liquid and particle combinations with the largest adsorption effects. For this reason, the properties of LiNO$_3$ and Al$_2$O$_3$ were used for this simulation. The results of the simulation using the modified mixing rule are displayed in Figure 10.

The trends in Figure 10 suggest a number of important parameters in thermally enhanced nanofluids. As mentioned earlier, the size of the nanoparticles plays a crucial role in any potential increases in thermal capacity. The substantial enhancement in heat capacity with particles below ~10 nm is consistent with reports in literature [3] and lends credibility to the accuracy of the model's approximations. Additionally, the thickness of adsorbed layer is an important parameter. While molecular dynamics simulations suggest that adsorption at the liquid-solid interface extends 1-3 nm from the solid surface [13], all of the current simulations are evaluated for relatively simple monatomic fluids. Studies suggest that more complex fluids may exhibit a thicker adsorbed layer [5]. These complex fluids will behave similar to the green or even black line in Figure 10 and demonstrate substantial improvements in effective heat

34

capacity over simpler fluids. A strong interaction (from Van der Waals and other forces) between the nanoparticle and the liquid will further increase the adsorbed layer thickness and have a similar impact on effective heat capacity.

In an ideal scenario, a complex fluid would be mixed with ~1 nm particles to yield the largest increase in effective heat capacity. However, in practice obtaining consistent 1 nm particles while avoiding agglomeration proves very difficult. Focusing on more complex fluids and strong liquid-particle attraction allows substantial improvements in effective heat capacity with reasonable particle sizes of around 10 nm in diameter.

2.3   SUMMARY

In this chapter, information from literature and modeling efforts were both used to isolate important parameters in engineering a nanoparticle HTF with an enhanced thermal capacity. Two scenarios were presented to predict the behavior of an adsorbed layer on the surface of nanoparticles. In the first scenario, the interfacial layer desorbed over a range of temperatures and resulted in an increase in effective heat capacity of the liquid nanofluids. The other case assumes a single desorption temperature for the adsorbed layer and results in an initial decrease in nanofluid heat capacity and a local peak corresponding to the enthalpy of desorption. Both instances have support in literature and the former is used as the focus of preliminary modeling. Although the first scenario was chosen to model, the important aspect of the analysis is to identify the particle size regime required for significant experimental adsorption effects. The model will predict similar parameters for the second scenario since the total enthalpy of desorption, the main parameter that influences particle size and adsorption layer thickness, is the same in both scenarios over the desorption temperature range. While the heat capacity as a function of temperature differs for the two cases, the total enhancement in effective thermal capacity is the same.

A novel modification to the classical mixing rule has been presented to account for the enthalpy associated with desorbing an interfacial layer. Several assumptions have been made to allow for the modified mixing rule to plotted while altering key variables. Trends in the data suggest important criteria for engineering an enhanced nanofluid:

1. Smaller nanoparticle sizes favor greater effective heat capacity. Particle sizes less than 10 nm in diameter are ideal. The key here is providing the maximum surface area for adsorption per unit mass of nanoparticle.

2. Avoiding nanoparticle agglomeration is crucial. Similar to the first point, any agglomeration will decrease the available surface area for adsorption. The use of surfactants may cause complications at high temperatures due to decomposition and may interfere with the adsorption phenomenon. Instead, small mass fractions of nanoparticles should be used to minimize risk of particle agglomeration.

3. Fluid-particle combinations that maximize the enthalpy of adsorption (resulting in a thicker adsorbed layer) are more favorable. Since the exact mechanism for this phenomenon is difficult to isolate, much of the optimization is left to trial and error. Literature provides two criteria for increasing the thickness of the interfacial layer: choose a fluid that is more complex than a simple monatomic fluid [5] and choose a particle that exhibits a strong attraction to the fluid [14].

4. Fluids that exhibit a large liquid temperature range before boiling or decomposing are desirable. With a larger liquid temperature range, there is a higher chance that the liquid-particle desorption energy will occur while the fluid is in a liquid state. This allows the adsorption behavior to be characterized experimentally and is crucial for the practicality of enhanced nanofluids.

These criteria will be used to help select favorable fluid and particle combinations in Chapters 3.

Chapter 3

3. Experimental Methodology

The experimental design of testing for enhanced heat capacity includes successful sample selection and preparation procedures as well as conducting experiments to confirm the existence of an adsorbed layer and quantity its thermal benefits. The experiments were conducted mostly with differential scanning calorimetry. X-ray diffraction and thermogravimetric analysis were used to further support the adsorption hypothesis. Transmission electron microscopy (TEM) was originally planned as a method of confirming properties of the nanofluids and adsorbed layer but proved to be prohibitively challenging. Difficulties with TEM imaging and recommendations for future improvements are found in Chapter 6.

3.1 SAMPLE SELECTION

Several fluid and particle combinations were chosen for the experiments based on the criteria outlined in Chapter 2 and information found in literature. The following nanofluids are summarized in Table 2. The sample preparation procedure varies with each of the nanofluids and will be discussed in Chapter 4.

For the nanoparticles, the key requirements are small average diameter, stability at high temperatures, and strong affinity to the adsorbate. Nanoparticles of SiO_2 and Al_2O_3 were chosen to satisfy these specifications. Reports in literature confirm that these ceramics have been shown to sustain an ordered adsorbed layer when in contact with certain liquids, making them a good candidate for the experiments in this thesis [14], [37]. SiO_2 nanoparticles with diameters ranging from 5 nm to 15 nm were procured from Sigma Aldrich. Al_2O_3 nanoparticles with 10 nm diameters as well as 200 nm diameters, in separate samples, were procured from Nanostructured and Amorphous Materials, Inc. The purpose of the larger particle sizes is to observe the difference in experimental results when the mass fraction of nanoparticles is held constant but the surface area available for adsorption (related to particle size) changes. This will help to elucidate the influence of particle surface area on the thermal capacity of nanofluids.

Several candidate fluids were selected as the focus of the nanofluid experiments. The first fluid was a high temperature carbonate eutectic, Li_2CO_3-K_2CO_3 with a 62:38 molar ratio. This eutectic has been used in several studies that report an increased heat capacity in nanofluids [3], [28], [31], [46] and is a natural choice for the experiments in this thesis. Another fluid used was Hitec HTS, a commercial molten salt used for CSP applications. The chemical composition is KNO_3-$NaNO_3$-$NaNO_2$ with a 44:7:49 molar ratio [20]. In addition to the practicality of increasing the thermal properties of a common commercial HTF, Hitec HTS has a lower melting temperature than Li_2CO_3-K_2CO_3 and as a result complications that arose when testing thermal properties at high temperatures were circumvented. While a high operating temperature HTF is valuable in increasing thermodynamic efficiency, feasibility and accuracy of thermal property measurements were a higher priority when evaluating the impact of adsorption at the particle interface and thus a lower temperature HTF was chosen. Finally, $LiNO_3$ was the last candidate fluid. While the melting temperature is higher than Hitec HTS, it is still within a reasonable testing range. Additionally, the other two candidates are eutectics and $LiNO_3$ avoids any issues that may arise from mixing and melting a eutectic salt. The results of these fluids combined with the previously mentioned nanoparticles are detailed in Chapter 4.

Table 2. Summary of nanofluid mixtures used in experiments.

Fluid	Melting Temperature	Particle	Particle Size	Particle Mass Fraction
Li_2CO_3-K_2CO_3	488°C	SiO_2	5 – 15 nm	1%, 2%
Hitec HTS (KNO_3-$NaNO_3$-$NaNO_2$)	141°C	Al_2O_3	10 nm	1%
$LiNO_3$	254°C	Al_2O_3	10 nm	1%, 2%
$LiNO_3$	254°C	Al_2O_3	200 nm	1%, 2%

3.2 DIFFERENTIAL SCANNING CALORIMETRY

A differential scanning calorimeter (DSC) is a piece of equipment used to measure the thermal capacity of a given sample. DSCs are typically used to measure enthalpy of a phase transformation, onset temperature of a phase transformation, and specific heat capacity. The essential function of a DSC is to measure the heat flux needed to change the temperature of a sample and the resulting data is interpreted to calculate the thermal storage properties. In

practice, a small furnace contains two sample stages, each with an embedded thermocouple to sense the temperature of the sample placed upon it as illustrated in Figure 11. Small hermetically sealed aluminum pans are placed atop each stage; one pan contains the sample of interest (~20 mg) and the other pan is empty and serves as a reference.
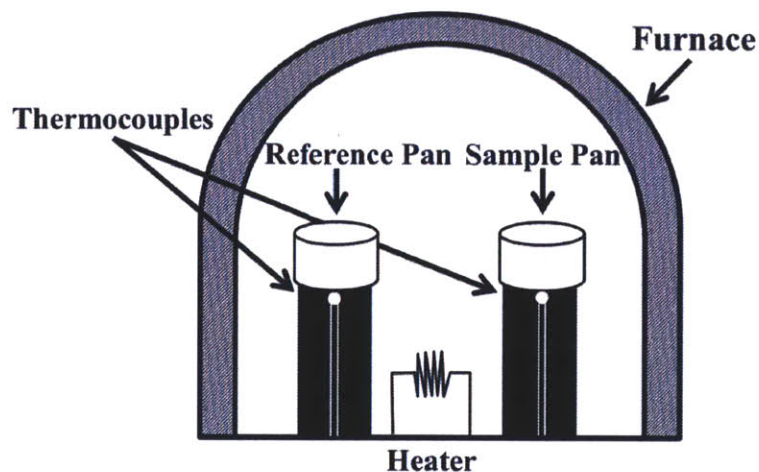
Figure 11. Simplified schematic illustrating the key components within a differential scanning calorimeter furnace.

When the data is processed, the thermal effects of the reference aluminum pan are subtracted from the signal. The user designates the temperature profile of the experiment using computer software. In most instances, this temperature profile is a simple constant ramp rate with isothermal periods at each end, illustrated in Figure 12. The DSC modulates the heat flux of the furnace to achieve the prescribed temperature profile in the sample stage thermocouple. The heat flux is recorded and used for the bulk of the data analysis. Throughout the experiment, the furnace is purged with nitrogen gas (or another inert gas) to maintain an inert environment. While the theory behind DSC measurements is relatively simple, accurate experiments are often difficult due to thermal drift in sensors, improper calibration, and furnace contamination. Experimental uncertainties of 5-10% are not uncommon in these measurements. For this reason, the experiments in this thesis were often run for 4 consecutive trials to gauge the consistency of the results.
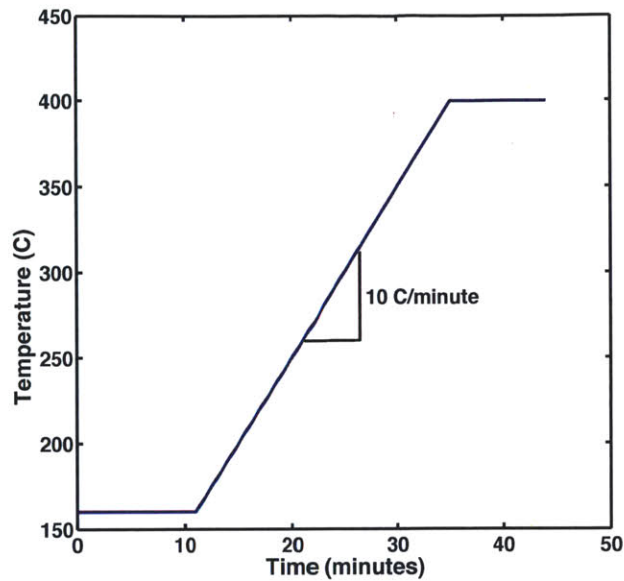
Figure 12. Common temperature profile used in DSC when measuring specific heat capacity and enthalpy of fusion.

The experiments in this thesis utilized two different DSCs. The first is a Mettler Toledo Polymer DSC R located in Professor Evelyn Wang's Device Research Laboratory at MIT and the second is a TA Instruments Q1000 DSC located in the Institute for Soldier Nanotechnology at MIT. The Mettler Toledo Polymer DSC R had a maximum operating temperature of 500°C and the TA Instruments Q1000 DSC had a maximum operating temperature of 550°C. The two calorimeters exhibited only minor differences in operation.
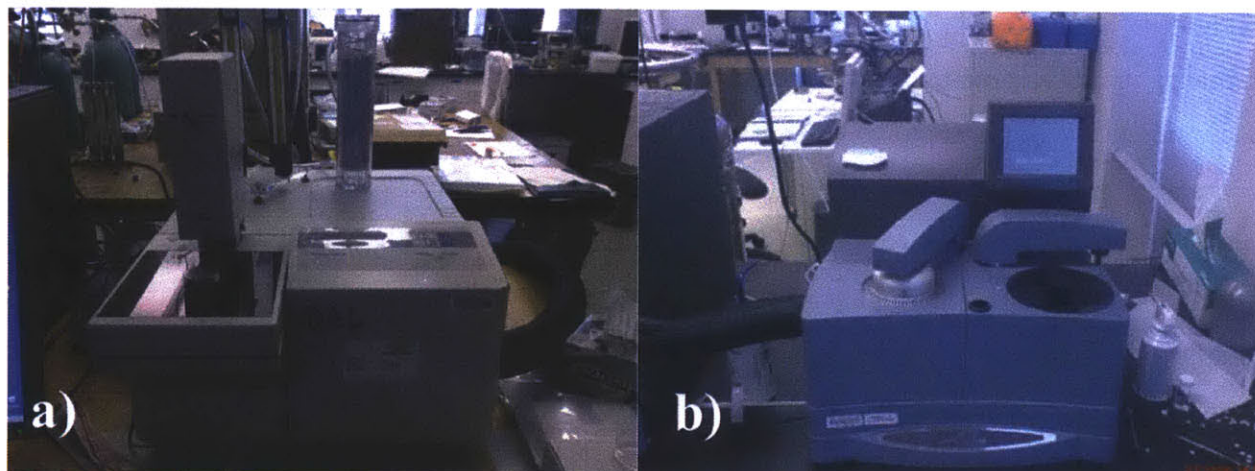
Figure 13. (a) Mettler Toledo Polymer DSC R (b) and TA Instruments Q1000 DSC.

3.2.1   Measuring Enthalpy of Fusion and Specific Heat Capacity

The guidelines for measuring enthalpy of fusion (latent heat) are detailed in the American Society for Testing and Materials' (ASTM) article E793-06 [22]. The procedure for this test is relatively straightforward. After calibration of the instrument, the sample is heated in the DSC at 10°C/min through its melting point to a stable temperature as illustrated in Figure 12. The resulting data, in Watts, is divided by the sample mass and, when plotted against time, will exhibit a clear peak indicating the phase transition. The integral of this peak, in J/g, is the enthalpy of fusion or latent heat of the sample.

The procedure for measuring specific heat capacity with differential scanning calorimetry is similar to that of enthalpy of fusion and described in ASTM article E1269-06 [24]. The sample is heated in the DSC at 10°C/min to 20°C/min through the temperature range of interest with a 5-10 minute isothermal period before and after the temperature ramp, shown in Figure 12. The same experimental procedure is conducted for a sapphire reference sample, a material with a well-characterized specific heat capacity. The specific heat capacity of the sample is determined by adjusting the heat capacity values of the sapphire standard according to the difference in recorded Wattages and sample weights. Further details about the calculations can be found in the ASTM standard procedure.

One of the major complications in DSC measurements is quantifying the uncertainty. While manufacturers report a heat flux accuracy of around 0.5%, the accuracy measurement is

conducted with a solid, metal sample, often indium, and heat capacity measurements of nonmetal, liquid samples are typically much less accurate. Traditionally, heat capacity measurements of liquid samples were accurate to ±10%. Modern calorimeters have improved the accuracy of heat capacity measurements to ±5% with more precise heat flow values and pans that provide better contact with the DSC thermocouples [47]. Although the accuracy of DSC measurements for liquid samples is rather poor, the average of the data from multiple trials of the same sample can be used to reduce uncertainty. This technique is utilized in Chapter 5 of this thesis.

3.3 X-RAY DIFFRACTION

X-ray diffraction (XRD) is generally used to identify the composition of a crystalline sample. X-ray intensity is measured in the sample as a function of the angle location of the x-ray detector. The measured intensities correspond to the distance between the atomic planes of the sample and are matched to a database with characteristic peak profiles of hundreds of crystalline structures [18]. While this technique is not often used for thermal analysis, it may be useful in determining the crystallographic structure of an adsorbed interfacial later. A heated sample stage was used to bring the nanofluid mixture above its melting temperature. Once the bulk of the liquid has melted, any crystalline structure of the adsorbed layer can be probed.

A Philips PANalytical X'PERT PRO diffractometer in the Center for Material Science and Engineering (CSME) at MIT was used in the experiments for this thesis. The XRD results will be discussed in Chapter 4.
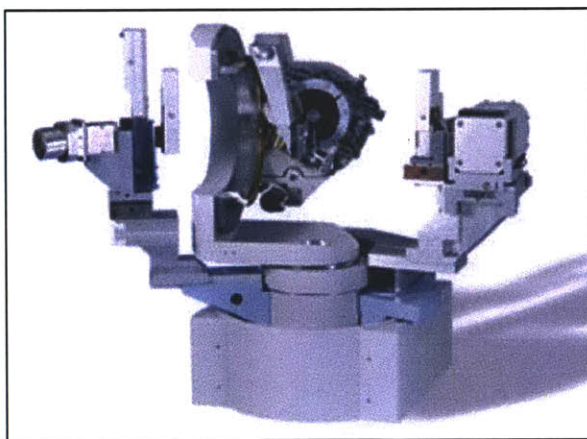
Figure 14. Philips PANalytical X'PERT PRO diffractometer used in experiments.

3.4   THERMOGRAVIMETRIC ANALYSIS

Thermogravimetric analysis (TGA) was used to verify the thermal stability of the $LiNO_3$ samples. TGA is a technique that precisely measures the mass of a sample using a microbalance as the sample is heated through a prescribed temperature profile. The change in mass as a function of temperature and time is recorded and can be useful when determining the desorption or decomposition behavior of a sample. The sample is loaded onto a platinum pan that hangs from a hook attached to the microbalance. The furnace is raised around the pan and the chamber is purged with nitrogen and helium gases throughout the course of the experiments to provide an inert atmosphere and remove any gases that are released from the sample. A TA Instruments Q50 Thermogravimetric Analyzer in the Institute for Soldier Nanotechnology at MIT was used in the TGA experiments.
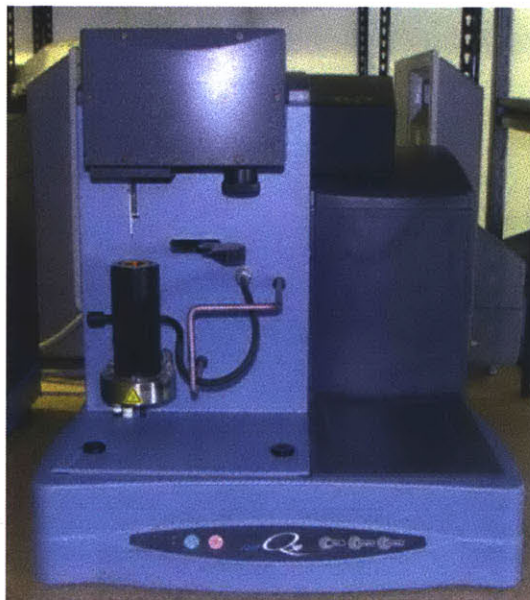
Figure 15. TA Instruments Q50 Thermogravimetric Analyzer used to confirm sample stability at elevated temperatures.

3.5   SUMMARY

After reviewing the key criteria for selecting fluid and nanoparticle combinations, several best candidates were chosen and are listed below:

1. Li_2CO_3-K_2CO_3 (62:38 molar ratio) with SiO_2 nanoparticles (5-15 nm)

2. Hitec HTS with Al_2O_3 nanoparticles (10 nm)

3. LiNO3 with Al_2O_3 nanoparticles (10 nm and 200 nm)

Additionally, differential scanning calorimetry, x-ray diffraction, and thermogravimetric analysis were discussed as useful experimental techniques for proving the existence of an adsorbed interfacial layer and assessing its impact on a fluid's thermal capacity.

4. Experimental Results

The nanofluid mixtures outlined in Table 2 were evaluated using DSC as well as XRD and TGA, when applicable. The sample preparation procedures and experimental results are described below.

4.1 LI_2CO_3-K_2CO_2 NANOFLUID RESULTS

The high temperature carbonate eutectic that has been featured in a number of studies proposing large experimental increases in heat capacity [3], [28], [31], [46] is the first fluid examined in this thesis.

4.1.1 Sample Preparation

The sample preparation of Li_2CO_3-K_2CO_3 (62:38 molar ratio) with SiO_2 nanoparticles closely follows the method outlined in literature [3]. First, 184.5 mg Li_2CO_3 and 211.5 mg K_2CO_3 were mixed with 4 and 8 mg of SiO_2 nanoparticles (5-15 nm) for 1% and 2% by weight particle concentrations, respectively. All of these materials were obtained from Sigma Aldrich. A pure carbonate eutectic without nanoparticles was also mixed. The mixtures were diluted with 60 mL deionized water and placed in an ultrasonicator for 2 hours. The mixtures were made in an aqueous solution to promote uniform dispersion of the nanoparticles while the sonication helps to dissolve the carbonates in the solution while helping to break up any agglomerated particles. After sonication, 20 mL of the solution was placed in a petri dish and set on a hot plate at 90°C overnight to evaporate the water in the sample. Avoiding boiling in the sample while evaporating the water was meant to help minimize particle agglomeration as noted in literature [3]. Once the water had evaporated, the dried carbonate nanofluid was scraped from the petri dish and used in DSC measurements.
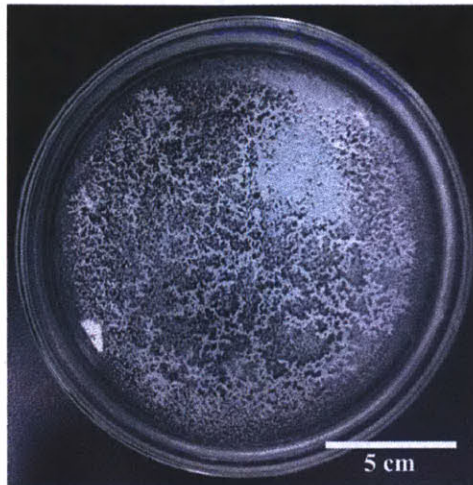
Figure 16. Li$_2$CO$_3$-K$_2$CO$_3$ eutectic with SiO$_2$ nanoparticles.

4.1.2 Differential Scanning Calorimetry Measurements and Results

The carbonate eutectic has a melting temperature of 488°C [3] and hence the TA Instruments Q1000 DSC (Figure 13 b) with a maximum operating temperature of 550°C was used. As per the ASTM standards for measuring specific heat capacity, the sample of Li$_2$CO$_3$-K$_2$CO$_3$ was held at 150°C for 8 minutes, ramped up to 550°C at 20°C/minute, held at 550°C for 8 minutes, and then ramped back down to 150°C at 20°C/minute, similar to the temperature profile shown in Figure 12. The last ramp down to 150°C is not part of the ASTM standard; however, it was included to prevent the DSC from cooling the sample to room temperature at a very rapid rate. Such a quick decrease in temperature was avoided as it might cause thermal contractions in the sample and pan, possibly degrading the pan's hermetic seal. The calculations for extracting specific heat values from the DSC data were performed on the temperature range of interest without any conflict with the ASTM standard.

The initial DSC results demonstrated trends consistent with literature reports [3], [28], [31], [46]. Figure 17 shows substantial increases in heat capacity of the nanofluids when compared with the pure carbonate eutectic. The Li$_2$CO$_3$-K$_2$CO$_3$ mixture with 1% SiO$_2$ nanoparticles showed an average increase in heat capacity of around 40% and the mixture with 2% SiO$_2$ nanoparticles exhibited an average enhancement of 100%. These initial results were very promising and a number of other studies were planned for various particle shapes and chemical compositions while maintaining Li$_2$CO$_3$-K$_2$CO$_3$ as the base fluid.
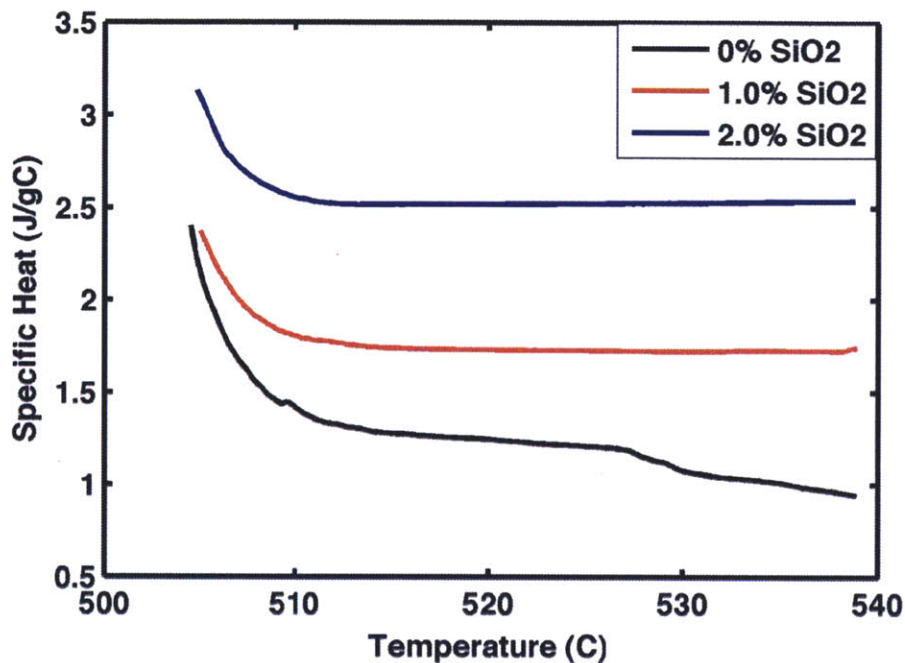
Figure 17. DSC results for heat capacity of Li₂CO₃-K₂CO₃ with different concentrations of SiO₂ nanoparticles. 1% and 2% by weight of SiO2 results in 40% and 100% increases in heat capacity, respectively.

However, the thermal properties of the pure Li_2CO_3-K_2CO_3 do not match the values that are expected from literature reports. The melting temperature of the carbonate eutectic is known to be 488°C and the heat capacity of the liquid phase is a constant 1.60 J/g°C [30]. In the DSC results, the melting point is closer to 500°C and the heat capacity in the liquid phase starts at 1.40 J/g°C before decreasing to 1.0 J/g°C as the temperature increases to 540°C. Without an accurate reproduction of the established thermal properties of the pure carbonate eutectic, it was difficult to have confidence in the increased heat capacity measurements of the SiO_2 nanofluids.

Additionally, complications arose when attempts were made to reproduce the initial enhancements in heat capacity. A new batch of Li_2CO_3-K_2CO_3 samples was mixed with the same procedure as the previous case. The pure eutectic and the 1% SiO_2 nanofluid were tested in the DSC using the same test procedure as the previous experiment. Each of the samples was run in the DSC three consecutive times and the results are displayed in Figure 18 with both plots displaying subsets of the larger data set.
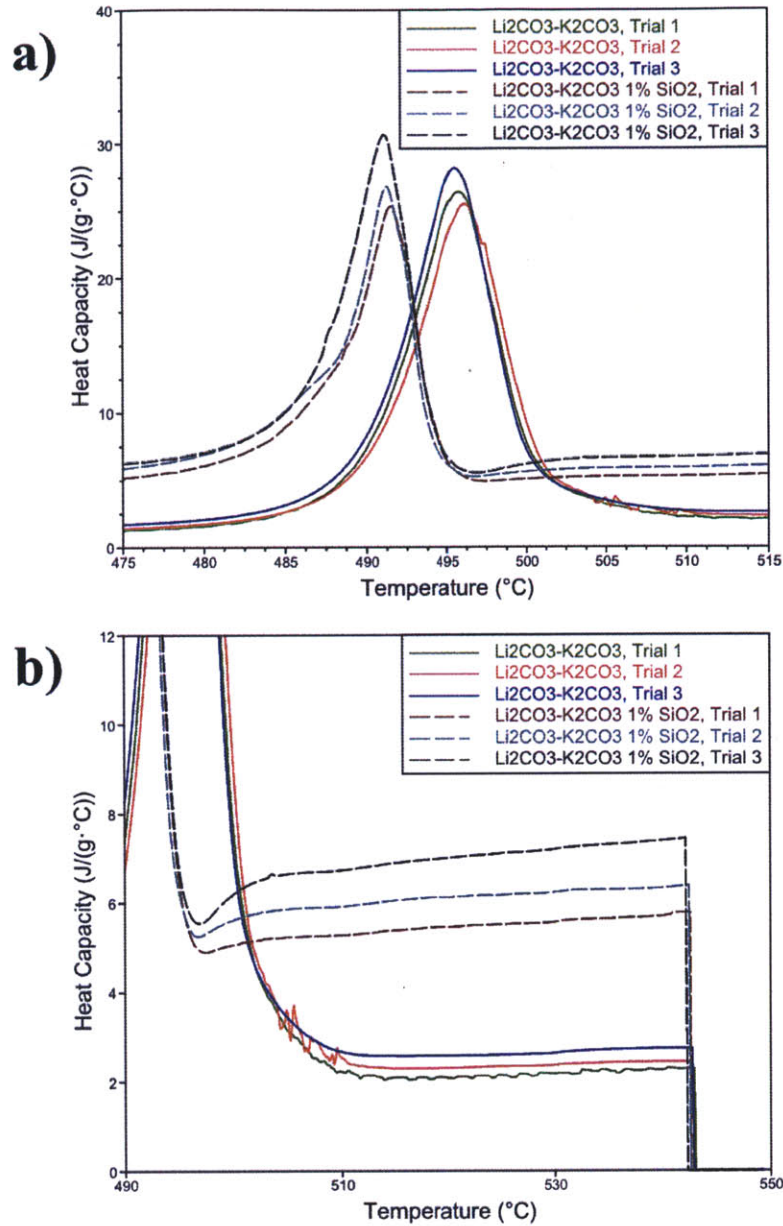
Figure 18. DSC results for heat capacity of pure Li_2CO_3-K_2CO_3 and Li_2CO_3-K_2CO_3 with 1% SiO_2 nanoparticles focusing on the (a) melting temperature and (b) liquid phase regions.

The first noticeable trend, as depicted in Figure 18 a, was the shift in the melting point of the nanofluid versus the pure eutectic. While reports in literature have discussed the manipulation of melting point of adsorbed layers, it is not expected that the presence of nanoparticles can shift the melting point of the entire nanofluid mixture. It was later revealed taht this behavior was characteristic of a DSC that is improperly calibrated near its maximum operating temperature.

48

Further evidence for the improper calibration can be seen in Figure 18 b. The heat capacity value of the pure carbonate eutectic was consistently higher than the 1.60 J/g°C value found in literature [30], the opposite of the behavior seen in the previous experiments. Even after calibration of the DSC, inconsistent results were observed in the high temperature range.

Additionally, subsequent trials with the same sample pan resulted in a significant change in the heat capacity of the sample. This behavior was indicative of mass loss in the sample pan. Mass loss was confirmed by weighing the pans with a mass balance before and after the DSC measurements. Although the DSC sample pans were labeled as hermetically sealed, it is likely that high-temperature experiments resulted in sufficiently high pressures within the pan and cause the hermetic seal to be compromised.

4.2 HITEC HTS NANOFLUID RESULTS

A fluid with a lower melting temperature was chosen as an appropriate test subject following the complications that arose when operating the DSC near its maximum operating temperature. Due to its prevalence in CSP applications, Hitec HTS, a KNO_3-$NaNO_3$-$NaNO_2$ mixture with a 44:7:49 molar ratio, was chosen as a candidate fluid with a more practical melting temperature of 141°C. The nanoparticle was also changed to 10 nm Al_2O_3 to further decrease the particle size from the 15 nm SiO_2 particles and to increase the available surface area for adsorption.

4.2.1 Sample Preparation

The sample preparation was similar to the carbonate eutectic with a modification made after the first batch in Section 4.1.1. Initially, 10 g Hitec HTS was mixed with 80 mL deionized water with one of the two samples containing 100 mg Al_2O_3 (10 nm) and the other left as pure Hitec HTS. The solutions were placed in an ultrasonicator for two hours to allow the nanoparticles to evenly disperse. Next, 40 mL of the solution was placed on a hot place at 90°C overnight and the water in the solution was allowed to evaporate. The first DSC experiments with the Hitec nanofluid displayed an anomalous peak in heat capacity values at 100°C in the first trial of each sample, seen in Figure 19. After the first trial, subsequent trials show little, if any, latent heat peaks at 100°C. This led to the conclusion that a small amount of water was left in the samples after the evaporation step. A change in the sample mass before and after the DSC measurements

supported this theory by indicating that some mass of water was leaving the sample pan during the experiment.
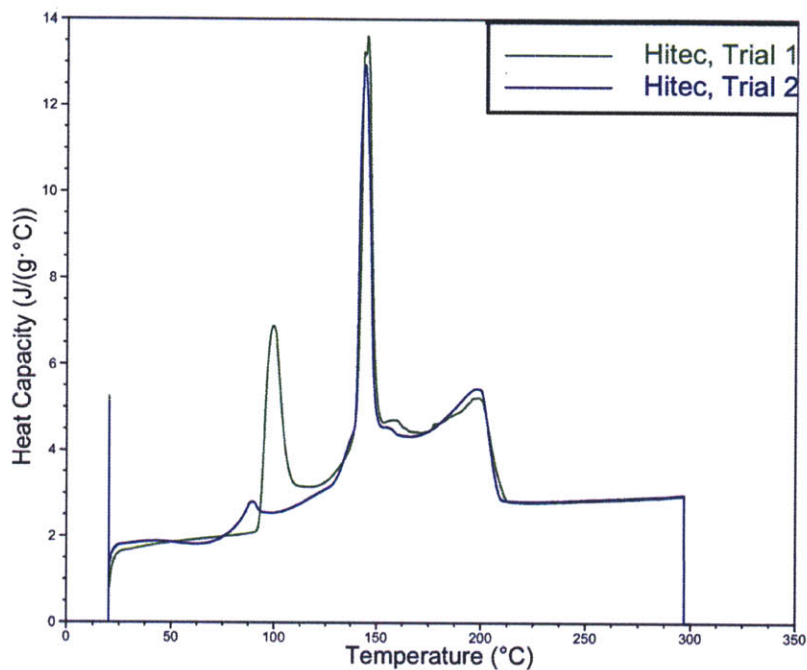
Figure 19. Heat capacity values for Hitec HTS showing residual water evaporating at 100°C in the first trial (green) of a given sample.

As a remedy, an extra preparation step was added to remove any residual water. After evaporating the bulk of the water at 90°C, the samples were continuously purged with nitrogen gas as the temperature was raised to 250°C and held at this temperature in nitrogen for one hour. DSC trials following this additional step did not show any anomalous heat capacity peaks at 100°C indicating that the residual water was removed from the sample.
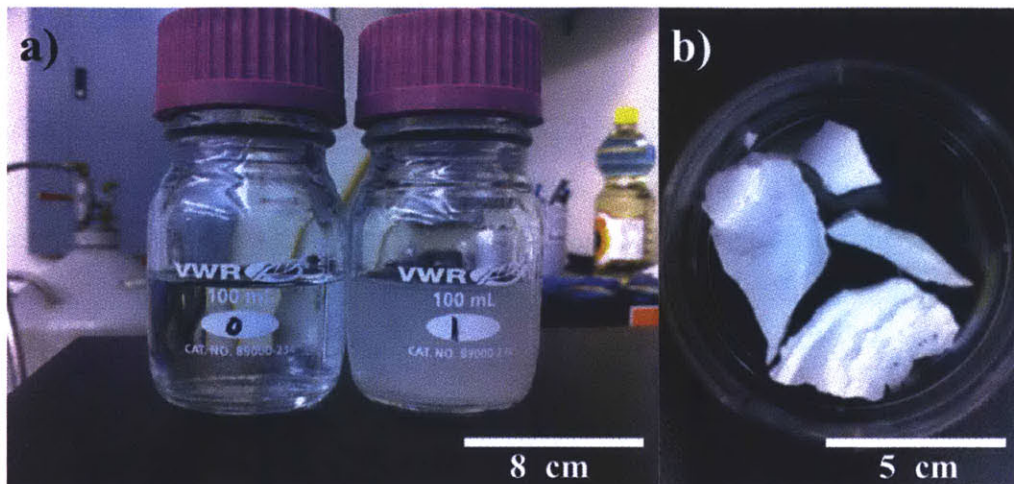
Figure 20. (a) Hitec HTS dissolved in water with (right) and without (left) Al$_2$O$_3$ nanoparticles. (b) Hitec HTS with embedded nanoparticles after preparation steps.

4.2.2 Differential Scanning Calorimetry Measurements and Results

A Mettler Toledo Polymer DSC R (Figure 13a) was used for measuring the heat capacity of the Hitec nanofluids. Instructions for proper operation of the Mettler Toledo DSC R are found in Section 7.2. While there were many issues involved with keeping the DSC calibrated properly, the Mettler Toledo software contains a special experimental method for gauging the calibration status of the DSC. A sample of Indium, an element with a well-characterized enthalpy of fusion, is heated through its melting point. The measured enthalpy of fusion and melting temperature are compared against the known values and the software issues a warning if the measured values deviate too far from the expected values. This calibration check was run before each of the Hitec nanofluid experiments in an attempt to minimize any complications related to calibration. The data presented in this section was obtained after a successful calibration check.

The adopted experimental methodology used follows the ASTM standard for measuring heat capacity. The samples were held at 20°C for 10 minutes, heated at 20°C/minute from 20°C to 400°C, and held at 400°C for 10 minutes, similar to the profile illustrated in Figure 12. In order to prevent the pans from losing their hermetic seal and leaking the sample into the DSC furnace, as was suspected in the carbonate eutectic studies, a small pinhole was made in the top lid of the sample pan. This pinhole allowed any atmospheric gases that may have been trapped in the pan to escape during the experiments. Although the pan was no longer sealed hermetically, there was

no sample mass lost through the pinhole and this technique is common practice for high temperature DSC measurements.

The heat capacity data for pure Hitec HTS and a mixture of Hitec HTS with 1% Al_2O_3 is shown in Figure 21. The main difference between the pure Hitec (black) and the nanofluid mixture (blue) is the absence of a small second peak in the nanofluid data. In the pure Hitec sample, this indicated that the mixture might not be a true eutectic and some constituents of the mixture were melting at their individual melting temperatures. Since Hitec HTS is a commercial product, its exact composition is proprietary and it is possible that it contains small quantities of components in addition to KNO_3, $NaNO_3$, and $NaNO_2$ to improve thermal stability at high temperatures. Additionally, little information exists in literature about the thermal behavior of Hitec HTS, so it is difficult to determine whether the several smaller latent heat peaks are characteristic of Hitec HTS or a result of how it was handled in the laboratory.
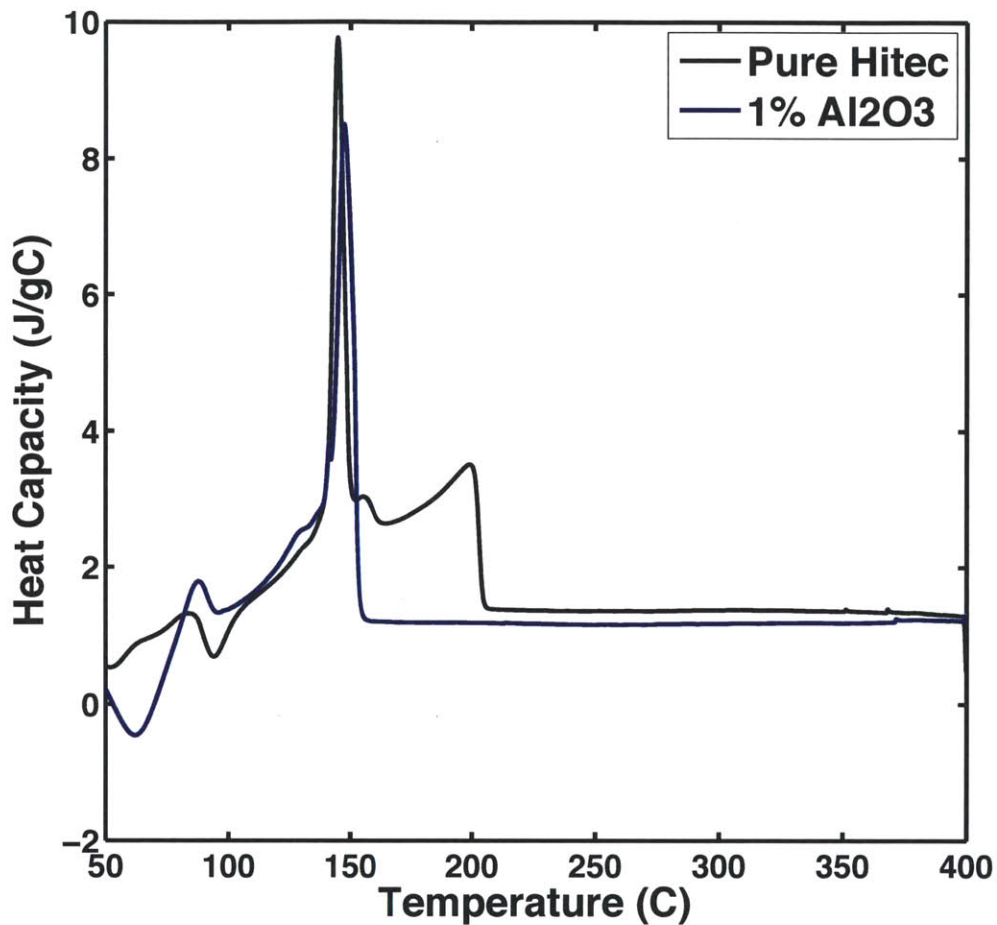
Figure 21. Heat capacity values of Hitec HTS with (blue) and without (black) 1% Al₂O₃ nanoparticles. The nanoparticle mixture exhibits a 35% suppression of the enthalpy of fusion.

Nonetheless, the suppression of the second peak resulted in a 35% decrease in the latent heat of the Al₂O₃ nanofluid. It is possible that suppression of latent heat and the decreased liquid heat capacity of the nanofluid are indicative of the second scenario described in Chapter 2 in which the interfacial layer remains completely adsorbed until some higher desorption temperature. The desorption temperature must be greater than 400°C, the limit of this DSC experiment.

While this scenario seems feasible, it became clear that Hitec HTS is not the best medium for investigating the fundamental thermal behavior of nanofluids. The uncertainty associated with the composition of Hitec HTS, its several latent heat peaks, its semi-eutectic behavior, and its strong sensitivity to adsorbed water (as demonstrated by the peaks and valleys at 100°C in Figure

21) make it difficult to attribute any changes in the thermal behavior of a Hitec HTS nanofluid to an adsorbed interfacial layer.

4.3   LINO₃ NANOFLUID RESULTS

The experimental complications related to Li_2CO_3-K_2CO_3 and Hitec HTS proved to be prohibitive when attempting to isolate the thermal capacity of the adsorbed interfacial layer. By choosing a simpler fluid, the influence of nanoparticles on eutectic formation can be eliminated to focus on the adsorption phenomenon. $LiNO_3$ was chosen for the remainder of the experiments as its low melting point of 254°C [45] lends itself to more reliable DSC measurements with the available DSC. Moreover, the melting temperature, enthalpy of fusion, and temperature-dependent heat capacity of $LiNO_3$ are well-characterized in literature [45], [48]. While $LiNO_3$ may not be the ideal candidate for practical high temperature HTF applications, it is an appropriate choice for exploring the thermal capacity of the adsorbed interfacial layer and the associated mechanisms at the nanoparticle surface.

4.3.1   Sample Preparation

The sample preparation for $LiNO_3$ was based on the procedure for Li_2CO_3-K_2CO_3 and Hitec HTS with additional steps to ensure that no residual water was contained in the samples. Samples were created with 10 nm Al_2O_3 as well as 200 nm Al_2O_3 in order to isolate the effect of available particle surface area on thermal capacity. The 200 nm Al_2O_3 mixture has an order of magnitude less surface area available for adsorption than the 10 nm Al_2O_3 mixture and lies outside the range of expected enhancement as described in Chapter 2.

First, 10 g $LiNO_3$, procured from Sigma Aldrich, was mixed with 100 mg Al_2O_3 (10 nm), 200 mg Al_2O_3 (10 nm), 100 mg Al_2O_3 (200 nm), and 200 mg Al_2O_3 (200 nm) in four separate mixtures to yield 10 nm and 200 nm mixtures with 1% and 2% by weight concentrations of nanoparticles. The particles were obtained from Nanostructured and Amorphous Materials, Inc. Each nanoparticle mixture and a pure $LiNO_3$ sample were diluted with 50 mL deionized water. The solutions were placed in an ultrasonicator for 3 hours to dissolve the $LiNO_3$ and prevent agglomeration of the nanoparticles. The resulting solutions are shown in Figure 22. 30 mL of each solution was placed on a hot plate at 90°C in a fume hood overnight to evaporate the

majority of the water from the sample. Next, the samples were placed on a hot plate at 400°C for 30 minutes while being continuously purged with nitrogen gas, as seen in Figure 23. A thermocouple was attached to the hot plate to read its temperature more accurately than the built-in controller.

Figure 22. LiNO$_3$ solutions with (from left to right) pure LiNO$_3$, 1% Al$_2$O$_3$ (10 nm), 2% Al$_2$O$_3$ (10 nm), 1% Al$_2$O$_3$ (200 nm), and 2% Al$_2$O$_3$ (200 nm).

Finally, the samples were placed in a vacuum oven at 3 kPa and 150°C overnight. The last two steps were necessary to remove any residual water in the samples, an issue that arose in many of the early DSC measurements of the LiNO$_3$ samples. In fact, the LiNO$_3$ samples demonstrated such a strong affinity to water that they were required to be stored in an airtight container to protect them from reacting with water vapor in the air.
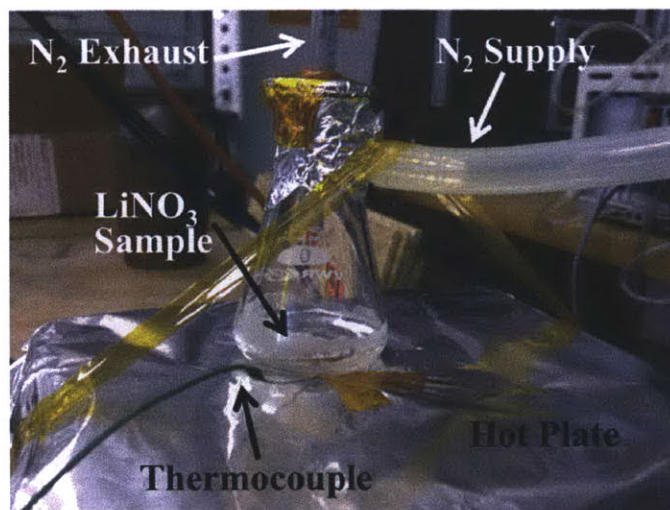
Figure 23. LiNO₃ nanofluids heated to 400°C while purged with N₂ gas during sample preparation.

4.3.2   Thermogravimetric Analysis Results

First, the water retention of the LiNO₃ samples was measured at an elevated temperature using the TGA. Early DSC measurements showed that the pure LiNO₃ samples (without nanoparticles) did not match the expected values of enthalpy of fusion and heat capacity that were reported in literature. Water retention in the sample was the most likely cause of this behavior. As a remedy, a vacuum oven step was added to the procedure. The TGA was subsequently used to determine if mass loss (likely due to retained water) occurred at the elevated temperatures used in the DSC. The temperature profile, seen in blue in Figure 24, held the sample at 100°C increments for 1 hour each until 400°C where it was held for 2 hours. In between the isothermal segments, the furnace was heated at 10°C/minute. The percentage of change in mass of the sample is plotted in green in Figure 24.
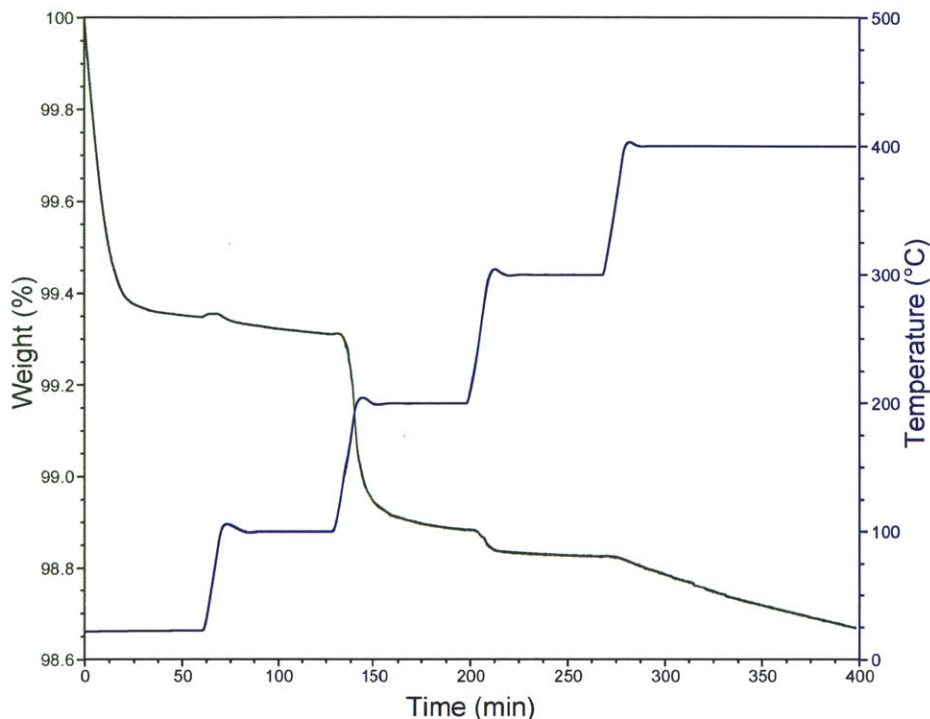
Figure 24. TGA results of LiNO₃ sample to test for water retention.

Over the course of the heating profile, the $LiNO_3$ sample lost only 1.3% of its total mass. This represents an insignificant amount of mass and indicated that any water retention by the sample was highly unlikely. This step validated the preparation procedure by indicating that all of the water added to the sample for the purpose of dispersing nanoparticles had been successfully evaporated.

The TGA was also helpful in establishing the decomposition behavior of $LiNO_3$. While it is reported in literature that most nitrate salts begin to decompose around 450°C-500°C [49], the exact decomposition temperature of $LiNO_3$ is not known. Additionally, the TGA proved useful in determining whether any decomposition of $LiNO_3$ occurred while preparing the sample (during the nitrogen purge at high temperatures, for example) by comparing its mass loss to a sample that did not undergo the preparation procedure.
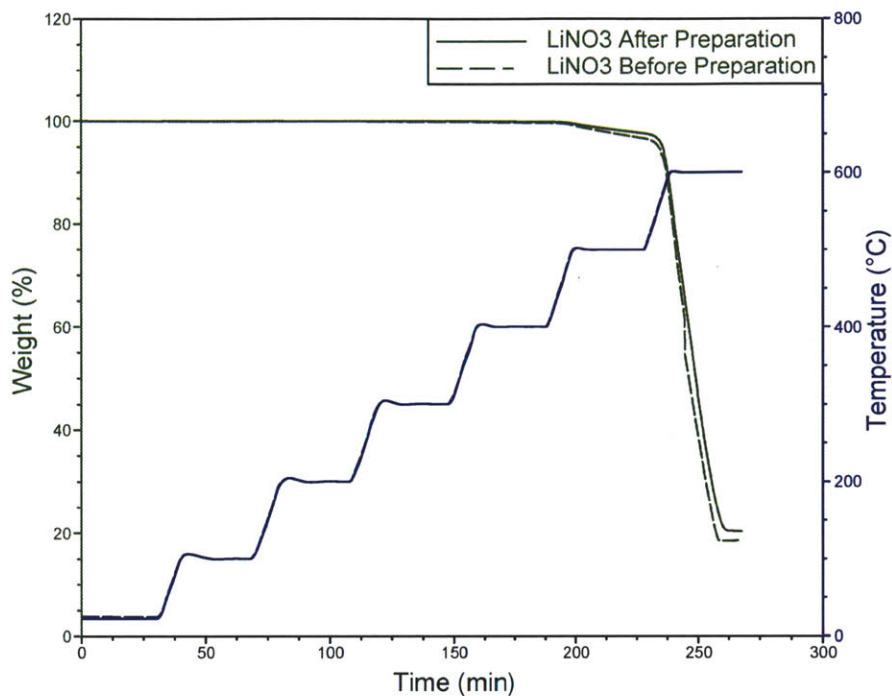
Figure 25. Decomposition of LiNO$_3$ in a TGA for samples taken before and after preparation procedure.

The experiments shown in Figure 25 follow a similar procedure to the water retention study with the isothermal temperatures reaching as high as 600°C. The TGA data indicated that LiNO$_3$ began minimal decomposition at 500°C while rapid decomposition occurred at 600°C. In order to avoid decomposition of the samples in the DSC, the maximum temperature should remain below 500°C. Additionally, the mass loss profiles for LiNO$_3$ before and after the nanoparticle preparation procedure (although no particles were added in the TGA studies) were nearly identical. This indicated that the prepared samples were just as stable at high temperatures as the unprepared LiNO$_3$ from the supplier and that the preparation procedure did not degrade the properties of LiNO$_3$.

4.3.3   Differential Scanning Calorimetry Results

The DSC measurements of the LiNO$_3$ samples were conducted using the TA Instruments Q1000 DSC. The ASTM standard for measuring heat capacity was again used to create the experimental procedure. Each sample was held at 160°C for 10 minutes, increased to 400°C at 10°C/minute, and held at 400°C for 10 minutes while being purged with N$_2$ gas at 50 mL/minute.

The TA Universal Analysis software converted the raw heat flux data into heat capacity values in accordance with the ASTM standard (Chapter 3.2.1) and a sapphire reference sample that was previously evaluated over the same temperature range.
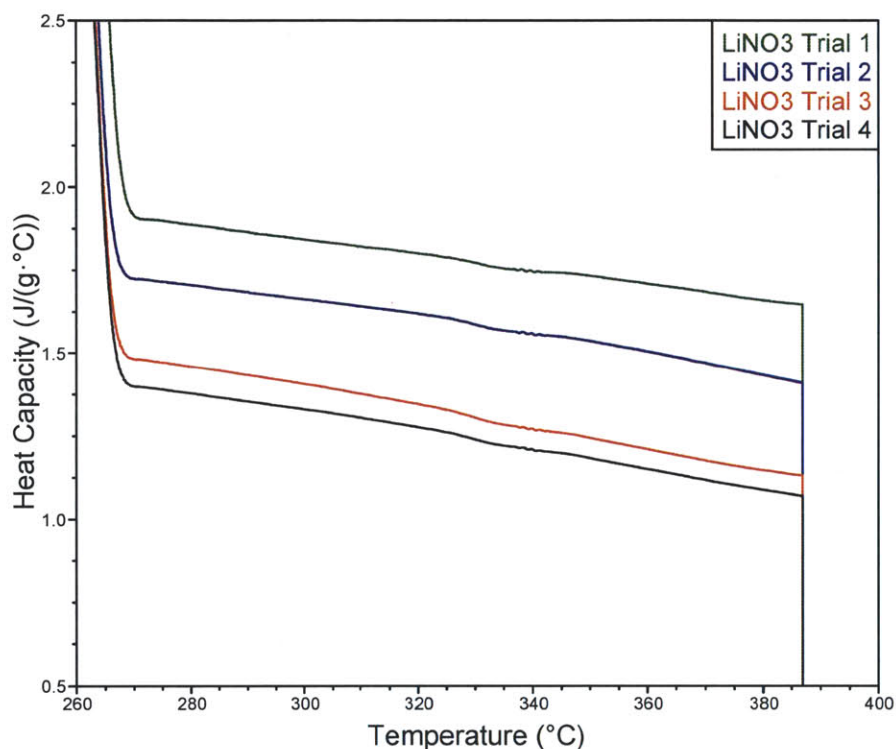
Figure 26. Erroneous behavior of LiNO₃ sample during heat capacity measurements. All four trials were conducted on the same sample and show a decrease in measured heat capacity with each subsequent trial.

After resolving the water retention issues in sample preparation, the DSC measurements of LiNO₃ samples were originally affected by the mass loss that affected the Li_2CO_3-K_2CO_3 and Hitec HTS samples. Even in the LiNO₃ samples that did not experience mass loss during DSC experiments, the heat capacity values from the DSC data decreased with each subsequent trial of the same sample of pure LiNO₃ as shown in Figure 26, a similar behavior to the pans that lost mass.

This behavior prevented reliable DSC data from being obtained, but was resolved upon further investigation. In DSC measurements, proper contact between the sample and the temperature sensor facing the bottom of the aluminum pan is crucial for accurate data. LiNO₃, as well as many other salts, exhibit low viscosities in their liquid phase. This causes the liquid

LiNO$_3$ to wick up the sides of the sample pan and leaving the bottom of the pan with a drastically reduced amount of sample (blue) in contact with the thermocouple (grey) below, as seen in Figure 27 a) and Figure 28 a).
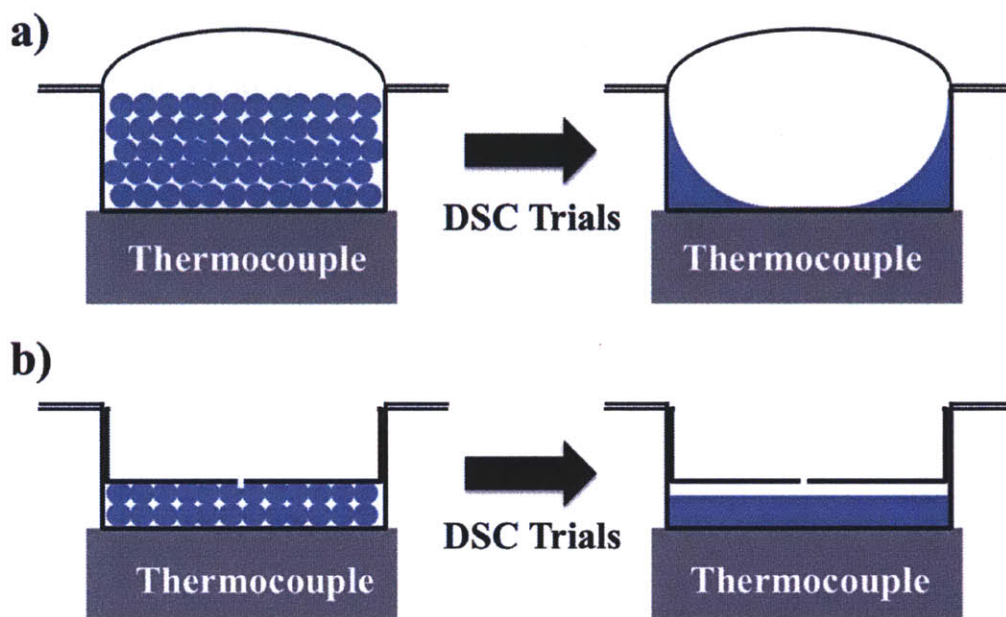
Figure 27. Schematic cross-section of (a) standard hermetic DSC pan and (b) Tzero hermetic DSC pan with micro-machined pinhole. Tzero pan suppresses wicking behavior that prevents good contact between the sample (blue) and the thermocouple (grey).

To resolve this issue, a new type of sample pan was used. The Tzero hermetic pans, shown in Figure 27 b) and Figure 28 b), suppresses any wicking of the fluid by utilizing a lid that keeps the sample in close contact with the bottom of the pan and thus the thermocouple on the sample stage. Additionally, the lids have a 75 µm micro-machined pinhole in the middle. This allows any gases originally trapped within the pan to exhaust at high temperatures without permitting the sample to escape the pan. The outgassing behavior relieves any elevated pressure inside the pan, preserving the seal between the lid and the pan, a common mechanism for sample loss in previous experiments.
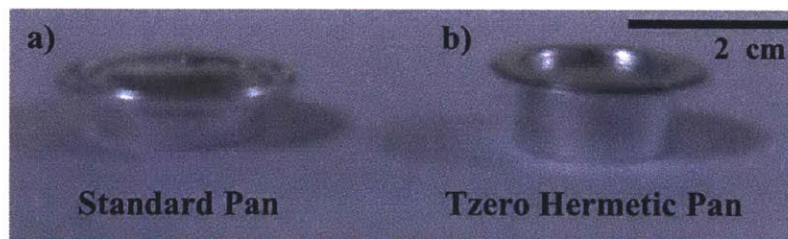
Figure 28. (a) Standard and (b) Tzero hermetic sample pans for TA Instruments Q1000 DSC.

With many of the experimental complications resolved, accurate and repeatable DSC measurements were made. Similar experiments that previously yielded a decrease in heat capacity with each subsequent trial of the same pure $LiNO_3$ sample (Figure 26) produced very consistent heat capacity values these new pans (Figure 29).
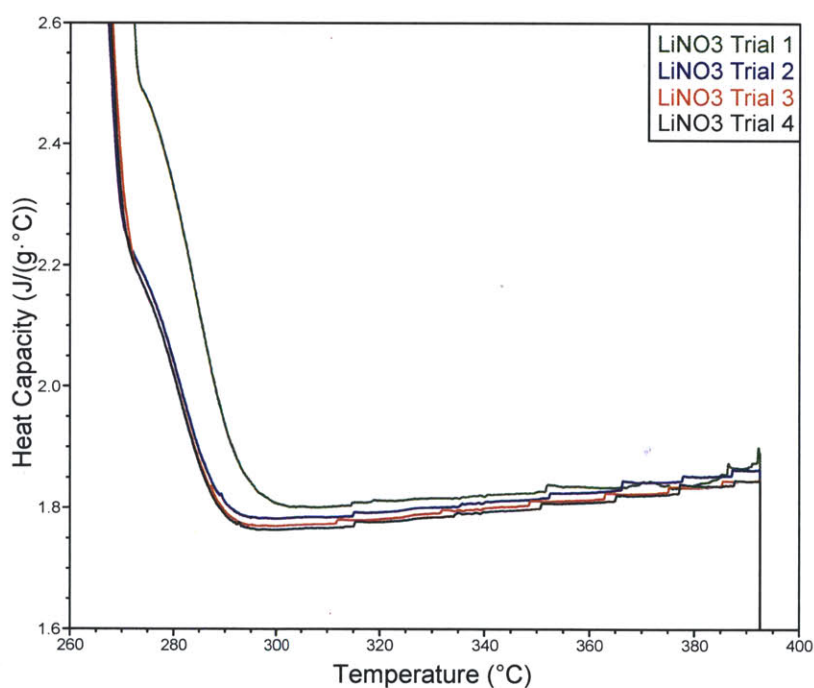
Figure 29. Consistent heat capacity values between multiple trials of the same sample using Tzero hermetic pans.

The slight increase in enthalpy of fusion in the first trial of $LiNO_3$ that can be seen at the left side of Figure 29 is indicative of the additional enthalpy involved with melting small granules of $LiNO_3$ powder when compared to melting a single block of $LiNO_3$, as is the case in the

61

subsequent studies once the original powder has melted and solidified. When analyzing the DSC data, the first trial of each sample was discarded to avoid such discrepancies.

Having obtained DSC results for pure $LiNO_3$ samples consistent with literature, the same experiment was performed with confidence on the samples with 1% and 2% of 10 nm and 200 nm Al_2O_3 nanoparticles. The results of the experiments are presented in Figure 30. The two samples with 10 nm particles exhibit a substantial decrease in heat capacity that scales with particle concentration while the 200 nm nanofluids exhibit only minor heat capacity enhancements over the pure $LiNO_3$ sample. Under the assumption that interfacial adsorption on the surface of the nanoparticles is playing a role, this is an expected behavior from the nanofluids. As illustrated in Figure 10, the 200 nm particles were too large for effects of the adsorbed layer to be significant at small particle mass fractions while the nanofluids with 10 nm particles were expected to show an anomalous change in effective heat capacity as is seen in Figure 30. The decrease in heat capacity of the 10 nm fluids suggests that the second scenario discussed in Chapter 2 is occurring; the interfacial liquid remains completely adsorbed to the surface of the nanoparticles and will desorb if raised to temperatures. The quantitative support for this argument based on the data from the DSC will be described in detail in Chapter 5.
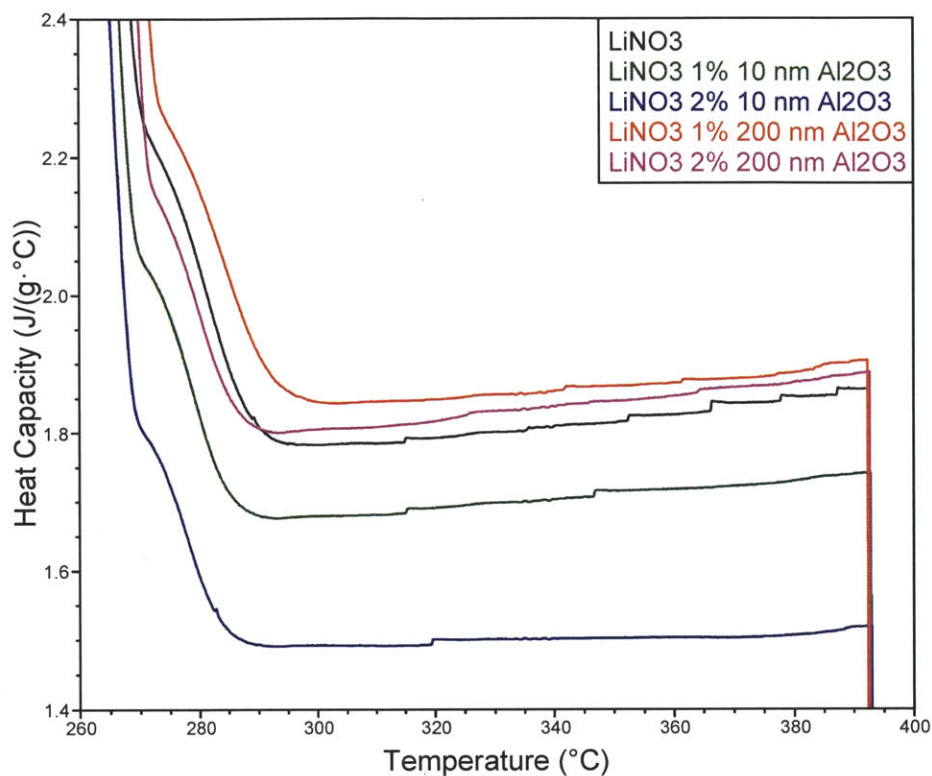
Figure 30. Heat capacity values of LiNO$_3$ with 1% and 2% of 10 nm and 200 nm Al$_2$O$_3$ nanoparticles.

While the quantitative analysis of the enthalpy of fusion from each of the fluids is also discussed in Chapter 5, the trends are not obvious from simple plots. Additionally, the liquid heat capacity of the pure LiNO$_3$ sample is approximately 1.8 J/g°C while the value found in literature is 2.0 J/g°C [45]. This small variation is likely due to a minor calibration issue in the DSC. The possibility that the decrease in heat capacity is due to decomposition of the LiNO$_3$ sample during the sample preparation has been ruled out as the TGA measurements in the previous section demonstrated that temperatures of 500°C to 600°C are required to initiate decomposition and these temperatures were not reached during the sample preparation.

4.3.4 X-Ray Diffraction

While XRD cannot provide information about the quantity of various sample constituents, it can be used to determine which crystallographic structures are present in a sample and the molecules that likely correspond to the detected structures. In this case, evidence of ordered

$LiNO_3$ on the surface of Al_2O_3 particles was investigated in a liquid $LiNO_3$ nanofluid. The Philips PANalytical X'PERT PRO diffractometer was used to scan the $LiNO_3$ sample with 1% 10 nm Al_2O_3 particles. A Cu radiation source was used and the sample was scanned from 10° to 70° at 25°C (solid sample) as well as 300°C (liquid sample).

The results of the room temperature scan are displayed in Figure 27 a) and the high temperature scan in Figure 27 b). Sharp peaks in the plots are indicative of ordered crystalline spacing and can often be matched with the peaks of known materials via several crystallographic databases. The measured data is in red while the database peaks for the sample constituents are indicated by vertical lines. Pure aluminum is included as a potential constituent because the sample holder is made of aluminum and may have been detected by the x-rays.

When comparing the two sets of data, a few trends shed light on the structure of the adsorbed interfacial layer. First, the $LiNO_3$ peak at 32° in the room temperature sample disappeared in the high temperature measurements. This indicated that $LiNO_3$ at high temperatures did not exist in the same crystalline structure as it did at room temperature. While this is obvious for the liquid component of the $LiNO_3$ sample, it means that the adsorbed layer does not exhibit the same structure as bulk solid $LiNO_3$. Given this information, three options are possible for the nature of the adsorbed $LiNO_3$: it does not exist at all, it is amorphous and will not show any diffraction peaks, or it exists in a state with a different density than standard solid $LiNO_3$ and thus has diffraction peaks that have not yet been characterized. Current literature suggests that the third option is the most probable as adsorbed liquid often exhibits a degree of ordering, likely closer to that of the substrate than the solid phase of the adsorbate [13].

Another trend in the data is that many of the database values for peaks in $LiNO_3$ are similar to those in Al_2O_3. This makes it difficult to distinguish which component each peak can be attributed to. Furthermore, it may even suggest that $LiNO_3$ and Al_2O_3 have a similar crystalline structure, an attribute that helps induce ordering at the liquid-solid interface. While the results of the XRD measurements are not as quantitative as those from the DSC, they have been used to elucidate the crystallographic structure of the adsorbed layer while showing agreement with predictions in literature.
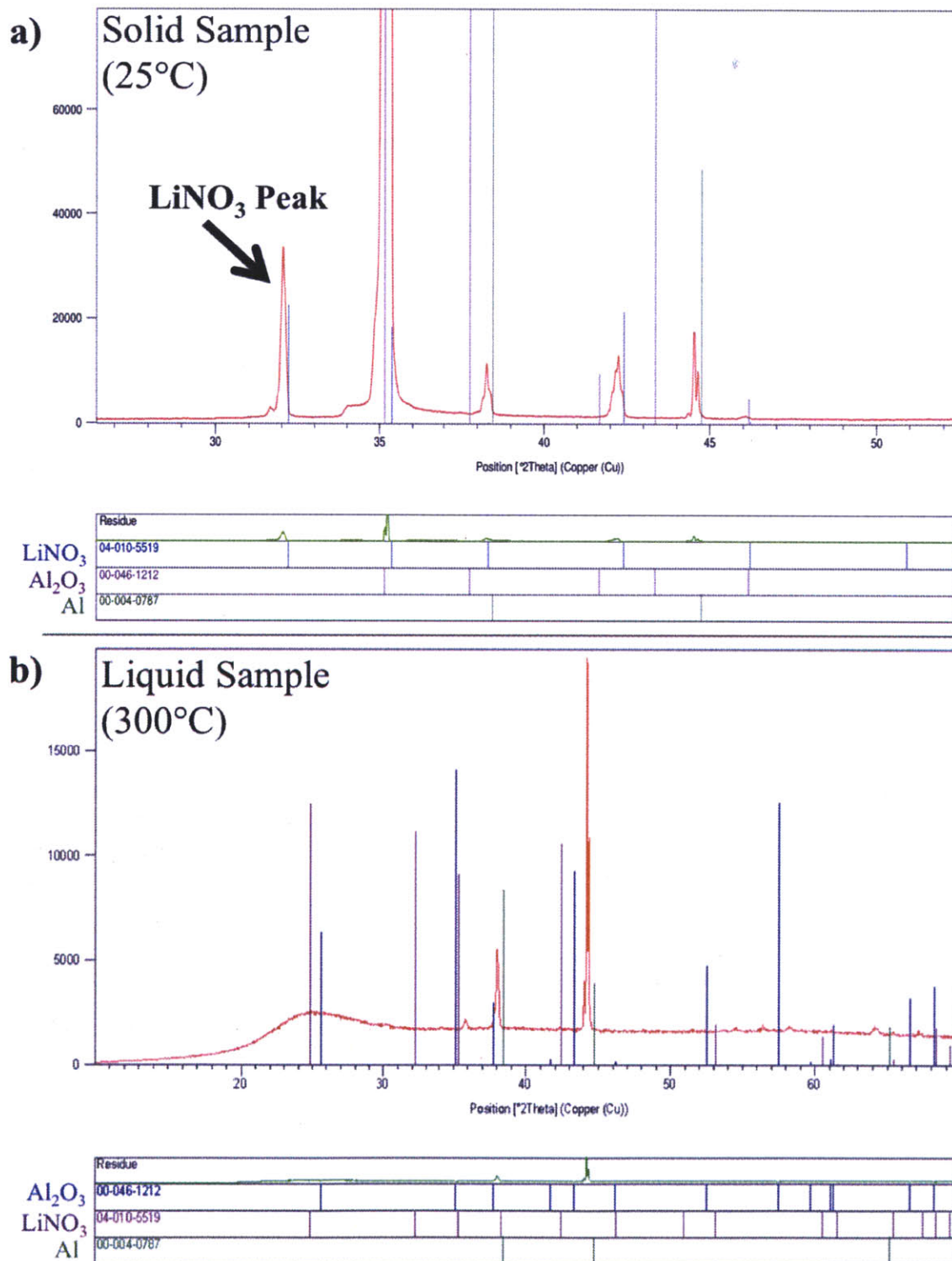
Figure 31. XRD scans of LiNO$_3$ with 1% 10 nm Al$_2$O$_3$ particles at (a) 25°C and (b) 300°C.

65

4.4 SUMMARY

Initial DSC experiments of Li_2CO_3-K_2CO_3 with 1% and 2% of 5-15 nm SiO_2 nanoparticles showed promising results with enhanced heat capacities that were consistent with reports in the literature. However, subsequent experiments revealed difficulties when operating the DSC near its maximum operating temperature of 550°C. A number of inconsistencies in data sets prevented any conclusions concerning apparent enhancement in heat capacity.

In an effort to produce more consistent results, Hitec HTS, a lower temperature fluid, was chosen for the heat capacity measurements. While many of the issues associated with high temperature DSC measurements were alleviated, Hitec HTS presented its own set of challenges. A substantial 35% decrease in enthalpy of fusion was measured in the Hitec HTS and Al_2O_3 nanofluid and may be a reflection of an adsorbed interfacial layer on the surface of the nanoparticles. Yet, the complex and enigmatic thermal profile of Hitec HTS makes it difficult to attribute this observation to the adsorption phenomenon.

In light of these experimental studies, it is clear that a simple, low-temperature fluid with well-characterized heat capacity and latent heat values is needed for more lucid experimental results. For this reason, $LiNO_3$ was chosen as a candidate fluid.

After finalizing the sample preparation procedure and resolving issues with low viscosity liquids in DSC sample pans, consistent DSC measurements were made for $LiNO_3$ samples with the addition of 1% and 2% of 10 nm and 200 nm diameter Al_2O_3 particles. Results were consistent with the single desorption temperature hypothesis presented in Chapter 2. Additionally, the necessity of small nanoparticles in observing the thermal implications of an adsorbed interfacial layer was verified experimentally. XRD was also utilized to investigate the crystalline structure of the $LiNO_3$ sample with 1% 10 nm diameter Al_2O_3 particles. The crystallography of the adsorbed layer was shown to be distinct from the crystalline structure of the bulk solid $LiNO_3$, either amorphous or an ordering closer to that of the Al_2O_3 particles.

5. Data Discussion and Analysis

The DSC data from LiNO$_3$ samples with 1% and 2% of 10 nm and 200 nm diameter Al$_2$O$_3$ particles in Figure 30 is consistent with the predictions for nanofluid behavior in Chapter 2 and warrants further analysis to understand the nature of the nanoparticle adsorption phenomenon. The 200 nm particle mixtures have heat capacity values nearly identical to pure LiNO$_3$ because the mass fractions of Al$_2$O$_3$ and adsorbed LiNO$_3$ are comparatively small. In contrast, the available surface area for adsorption in the 10 nm particle solutions is sufficiently high that the mass of the adsorbed layer is on the order of the mass of the remaining liquid LiNO$_3$. The transition to significant adsorption effects in the 10 nm particle regime validates the assumptions in Equation 5 and Figure 10 used to predict the required particle size. Namely, the experimental data verifies the assumption that the enthalpy of desorption and the enthalpy of fusion of the liquid are the same order of magnitude.

The data from the 10 nm particle samples is investigated to determine if the nanoparticle adsorption theory can reasonably explain the anomalous decreases in heat capacity values and if so, what the data reveals about the nature of the adsorbed interfacial layer.

5.1   EXPERIMENTAL RESULTS AND THE TRADITIONAL MIXING RULE

The first step in declaring the heat capacity results of the 10 nm particle mixtures anomalous is to prove that the data deviates from predictions made using current modeling theory. To accomplish this, the experimental data was plotted against a simple mixing rule for calculating the heat capacity of a particle mixture (Equation 2) and the results are displayed in Figure 32. The temperature dependent properties of LiNO$_3$ [45] and Al$_2$O$_3$ [50] were obtained from literature.

The deviation of the experimental values of pure LiNO$_3$ from those found in literature is most likely due to DSC calibration issues. Since the possibility of decomposition of the LiNO$_3$ samples was largely discredited in the TGA results in Chapter 5, calibration of the DSC with improper sample pans would have cause this small drift from accepted values. Although the

difference between the experimental and literature values of heat capacity highlights the large systematic error common for DSC heat capacity measurements of ±5% [47], the repeatability of the experiments was within 2% between trials of each sample indicated low random error. With low random error, the relative difference between the measurements for each of the nanofluids can be compared with confidence. Further, the systematic error and random error of the enthalpy of fusion measurements for the same samples was less than 1%. Both heat capacity and enthalpy of fusion measurements for $LiNO_3$ with 10 nm Al_2O_3 nanoparticles exhibited anomalous decreases from pure $LiNO_3$ measurements that were outside the range of experimental uncertainty.

The true utility of the comparison in Figure 32 is the confirmation that the decrease in the heat capacities of the nanoparticle mixtures is a result of more than simply the particles themselves. The anomalous reduction in heat capacity of the nanofluids is presumed to be the result of an adsorbed $LiNO_3$ layer on the surface of the nanoparticles that exists in a compressed state (with a lower effective heat capacity) and will desorb at a higher temperature, joining the bulk of the $LiNO_3$ in the liquid phase.
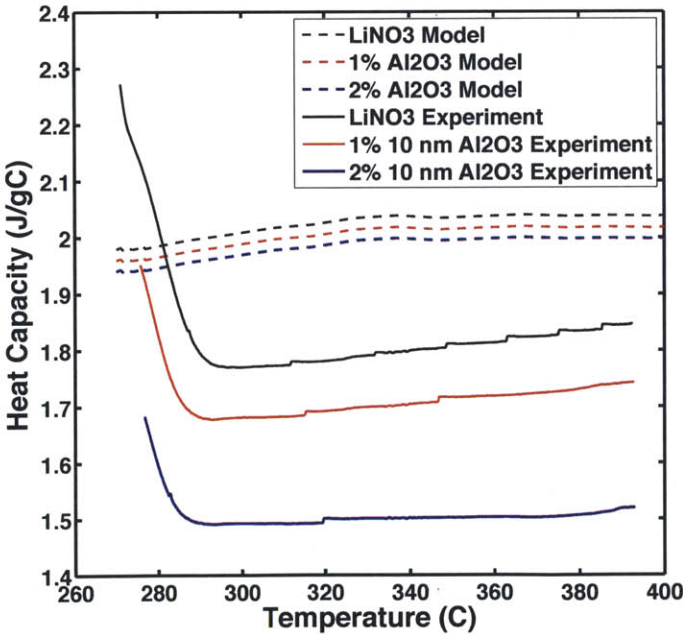
Figure 32. Heat capacity values for LiNO3 nanofluids (solid) compared to predictions from the traditional mixing rule (dashed).

5.2 QUANTIFYING ADSORBATE MASS

As mentioned in the modified mixing rule in Chapter 2 (Equation 5), the mass of nanofluid mixtures can be described as the sum of three components: the bulk fluid, the particle, and the adsorbed fluid layer, shown in Equation 6.

$$m_{nanofluid} = m_{bulk} + m_{particle} + m_{adsorbed} \qquad (6)$$

The difference in the DSC data of the nanofluids from the pure $LiNO_3$ samples was used to estimate the mass of the adsorbed fluid layer in the 1% 10 nm Al_2O_3 fluid and the 2% 10 nm Al_2O_3 fluid, where the adsorbed mass was expected to be significant. Since reductions were observed for the enthalpy of fusion as well as the heat capacity (latent and sensible heat) of each sample, there are two mechanisms for approximating the mass of the adsorbed layer, $m_{adsorbed}$. Once obtained, these approximations can be compared to each other for consistency and to the literature for feasibility.

The approximation of the mass of the adsorbed liquid using enthalpy of fusion values is straightforward. The enthalpy of fusion values for the 1% and 2% 10 nm Al_2O_3 nanofluids were obtained by integrating the heat flux signal from the DSC as described in the ASTM standard. Since small variations occurred in these enthalpy values, the enthalpy values from the second, third, and fourth trial of each sample were averaged to obtain accurate values (standard deviation was ~1% of the average enthalpy value). The average enthalpy of fusion values were multiplied by the total sample mass and equated to the product of the accepted value of enthalpy of fusion for $LiNO_3$ and the mass of the bulk (melted) $LiNO_3$, the unknown in the Equation 7. This equation sets the total heat flux measured in the melting region of the nanofluid to the effective mass of $LiNO_3$ that the flux value is able to melt.

$$m_{nanofluid} h_{fg,nanofluid} = m_{bulk} h_{fg,LiNO3} \qquad (7)$$

Once m_{bulk} is calculated, $m_{adsorbed}$ can be determined from Equation 6. The mass fraction of the adsorbed layer, γ, is defined in Equation 4 and is useful when comparing the results. For the

1% 10 nm Al$_2$O$_3$ and 2% 10 nm Al$_2$O$_3$ data, γ = 8% and γ = 16%, respectively. The twofold increase in adsorbed mass is exactly what is expected when doubling the particle concentration if equal levels of agglomeration are assumed.

A similar approach was taken to approximate the mass of the adsorbed layer by the change in heat capacity values. The liquid heat capacity values were averaged over three trials of each sample as described in the previous approximation. Equation 8 was used to predict m_{bulk} and is the sensible heat analogy to Equation 7 that equated latent heat values.

$$m_{nanofluid}C_{P,nanofluid} = m_{bulk}C_{P,LiNO3Liquid} + m_{particle}C_{P,particle} + m_{adsorbed}C_{P,adsorbed} \qquad (8)$$

This approximation is expected to be slightly less accurate for two main reasons. The first is that it the heat capacity of the adsorbed layer, $C_{P,adsorbed}$, is unknown. Since the density of the adsorbed layer is expected to be similar to that of solid LiNO$_3$, the heat capacity value of solid LiNO$_3$ was used as an approximation. However, density functional theory predicts that the density of the adsorbed layer is higher than the solid phase of the adsorbate as illustrated in Figure 5. A higher density solid typically results in a lower heat capacity from less molecule mobility as demonstrated by the lower heat capacity of diamond compared to graphite [50]. By using a heat capacity value that underestimates the actual value for the adsorbed layer, it is expected that the heat capacity approximation slightly underestimates the mass of the adsorbed layer, an issue that is not a concern in the enthalpy of fusion approximation.

Additionally, the sensible heat approximation is not based on an absolute value and thus must be evaluated at a specified temperature. In this case, the approximation was evaluated at 350°C. From m_{bulk}, γ was calculated for each fluid. For the 1% 10 nm Al$_2$O$_3$ and 2% 10 nm Al$_2$O$_3$ data, γ = 4.6% and γ = 14.2%, respectively. While these approximations are lower than the enthalpy of fusion values, they are the same order of magnitude and reasonably close given the shortcomings of the sensible heat approximation. Smaller mass fractions than the enthalpy of fusion approximation are expected as the mass of the adsorbed layer was underestimated due to the uncertainty in the heat capacity of the adsorbed layer.

The approximations for the mass of the adsorbed layer in the nanofluids provide insight into the potential thermal benefit from the enthalpy of desorption. The experimental decrease in enthalpy of fusion of the nanofluid is expected to be due to the fluid that remains adsorbed to the

surface of the nanoparticle that will desorb at a higher temperature as illustrated in Figure 9. The enthalpy of desorption is expected to be higher than the enthalpy of fusion of the fluid due to the particle-fluid interaction being stronger than the fluid-fluid interaction for fluid molecules close to the particle surface, a requirement for adsorption. With an estimate of the mass fraction of adsorbed fluid, the lower bound for the enthalpy of desorption is known and quantified in Equation 9.

$$h_{adsorption} > \gamma h_{fg,LiNO3} \tag{9}$$

Using the values for adsorbed mass fraction, γ, obtained with the heat of fusion approximation above, the enthalpy of adsorption, $h_{adsorption}$, is estimated to be greater than 28 J/g and 56 J/g for $LiNO_3$ with 1% and 2% mass fractions of 10 nm Al_2O_3 particles, respectively. This enthalpy represents the increase in thermal capacity that can potentially be harnessed if the desorption temperature lies within the useful operating temperature range of the nanofluid. In typical PCM-enhanced fluids, a PCM such as n-octadecane provides 12 J/g of additional thermal capacity at 10% mass concentration in the fluid [23]. The enhancement in thermal capacity is potentially significantly greater for fluids that harness adsorption on the surface of solid nanoparticles than fluids with PCMs provided that desorption occurs at a reasonable temperature.

5.3   APPROXIMATING ADSORBED LAYER THICKNESS

In order to compare the mass fraction of the adsorbed layer to previous studies of adsorption at the solid-liquid interface, the values must be translated from mass fraction to the thickness of the adsorbed layer. This is possible by using a geometric argument and a few simple assumptions. First, Figure 33 illustrates a number of variables that will be used in the approximation: r_{in} is the outer radius of a nanoparticle (blue), r_{out} is the distance from the center of the nanoparticle to the edge of the adsorbed layer (red), and $t_{adsorbed}$ is the thickness of the adsorbed layer.
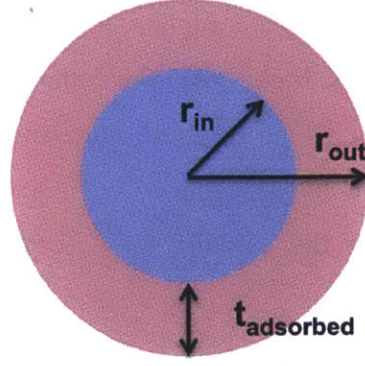
Figure 33. Variables describing nanoparticle size (blue) and adsorbed layer thickness (red).

The argument for the thickness of the adsorbed layer as a function of adsorbed layer mass is as follows. The mass of the adsorbed fluid can be written in terms of the number of particles, $n_{particle}$, the density of the adsorbed layer, $\rho_{adsorbed}$, and the respective radii, as seen in Equation 10.

$$m_{adsorbed} = \rho_{adsorbed} V_{adsorbed} = \rho_{adsorbed} n_{particle} \frac{4}{3} \pi (r_{out}^3 - r_{in}^3) \qquad (10)$$

Next, the number of particles is written as a function of the mass and density of the particle, both of which are known.

$$n_{particle} = \frac{V_{particle}}{\frac{4}{3}\pi r_{in}^3} = \frac{m_{particle}}{\frac{4}{3}\pi r_{in}^3 \rho_{particle}} \qquad (11)$$

Combining Equation 10 and Equation 11 yields Equation 12 for the mass of the adsorbed layer.

$$m_{adsorbed} = m_{particle} \frac{\rho_{adsorbed}}{\rho_{particle}} \frac{r_{out}^3 - r_{in}^3}{r_{in}^3} \qquad (12)$$

72

Equation 12 can be solved for r_{out} and written in terms of the thickness of the adsorbed layer, $t_{adsorbed}$. In Equation 13, ϕ is the mass fraction of the nanoparticles as defined in Equation 3.

$$t_{adsorbed} = r_{out} - r_{in} = \sqrt[3]{\frac{m_{adsorbed}}{\phi m_{nanofluid}} \frac{\rho_{particle}}{\rho_{adsorbed}} r_{in}^3 + r_{in}^3} - r_{in} \qquad (13)$$

In order to solve for adsorption layer thickness, the density of the adsorbate, $\rho_{adsorbed}$, is assumed to be the density of the solid phase of $LiNO_3$, a value that mimics the compressed, ordered nature of the adsorbed layer. In future work, the density of the adsorbed layer could be better approximated with MD simulations and possibly environmental transmission electron microscopy. The largest assumption inherent in this model is that the nanoparticles do not agglomerate and their entire surface area is available as an adsorption site. Significant particle agglomeration will increase the effective particle size and ultimately decrease the mass fraction of the adsorbed layer. However, any reduction in surface area from agglomeration is expected to be minimal at low particle mass fractions and a small amount of error is permissible. The agglomeration assumption can be verified or refined through use of an environmental transmission electron microscopy measurement detailed in Section 6.2.3.

The results of Equation 13 with the enthalpy of fusion and heat capacity approximations for the mass of the adsorbed layer are shown in Table 3. The uncertainty represents a 10% variation in particle diameter.

Table 3. Estimates of adsorbed layer thickness based on analysis of DSC data.

Mass fraction of Al2O3 Particles (10 nm)	Enthalpy of Fusion Approximation	Heat Capacity Approximation
1%	$t_{adsorbed} = 7.1 \pm 0.6$ nm	$t_{adsorbed} = 5.3 \pm 0.5$ nm
2%	$t_{adsorbed} = 7.1 \pm 0.6$ nm	$t_{adsorbed} = 6.7 \pm 0.6$ nm

The estimates for adsorbed layer thickness show reasonable agreement between the enthalpy of fusion approximations and the heat capacity approximations. This lends credibility to the assumption that the two methods of approximation are indeed measuring the same phenomenon. Further, the predicted thicknesses of the adsorbed layer are on the same order as what has been

reported in literature, both in MD simulations and in TEM images [13], [51]. The agreement with literature increasingly supports the hypothesis concerning the adsorbed layer playing a significant role in the LiNO$_3$ samples. While the reported adsorbed layer thicknesses are typically 1-3 nm, these studies used simple, monoatomic fluids. In larger molecules, such as LiNO$_3$, it is predicted that the adsorbed layer thickness may extend well beyond 3 nm [5]. This agreement with the current, accepted knowledge of adsorption at the liquid-solid interface greatly increases the confidence that this phenomenon is occurring in the LiNO$_3$ samples.

5.4   SUMMARY

After carefully analyzing the data obtained from the DSC measurements of LiNO$_3$ samples with 1% and 2% of 10 nm and 200 nm diameter Al$_2$O$_3$ particles, several trends in the data have been justified. While the 200 nm samples exhibit minimal deviations from the pure LiNO$_3$ sample, the 10 nm samples have been shown to have heat capacity values that are drastically lower than that predicted by the traditional mixing rule in Chapter 2 for small particle sizes. Moreover, the magnitude of the decreased thermal values were quantified and attributed to a significant mass fraction of the adsorbed interfacial layer on the surface of the nanoparticles. Approximations using the decrease in enthalpy of fusion as well as the heat capacity resulted in similar estimates of γ, the mass fraction of adsorbed LiNO$_3$. In practice, this adsorbed mass fraction also represents the theoretical amount of additional thermal capacity that will be available at the higher desorption temperature and is as high as 16% of the total enthalpy of fusion (56 J/g).

A geometric model was used to predict the thickness of the adsorbed layer from the mass fraction of adsorbed LiNO$_3$ as determined from the DSC data. The results showed a thickness of 5.3 nm to 7.1 nm, values that are consistent with what is expected from simulations and experiments in literature. The analysis of the DSC measurements makes a strong case for the existence of an adsorbed layer in the nanoparticle mixtures and contributes novel estimations for the adsorbed layer thickness in complex molecules, a value that has only been reported for simple, monatomic fluids.

6. Conclusions and Future Work

This thesis has explored the thermal capacity of high temperature HTFs aimed at increasing the efficiency of CSP systems. To avoid the issues associated with PCM mixtures, adsorption at the liquid-solid interface has been investigated as a mechanism for enhancing the thermal capacity HTFs. While this adsorption phenomenon has been investigated in various studies, none report its potential to serve as a medium for thermal storage.

Small fractions of solid ceramic nanoparticles serve as active sites for adsorption in molten salt nanofluids; the desorption of this interfacial layer at high temperatures provides a mechanism for storing enthalpy, similar to the enthalpy of fusion during phase change. After consulting literature and modeling the potential enhancement in these nanoparticle mixtures, several fluid and particle combinations were selected for experimental investigation using DSC, XRD, and TGA techniques as appropriate. Li_2CO_3-K_2CO_3, Hitec HTS, and $LiNO_3$ were used as base fluids with 1% and 2% by mass of SiO_2 (15 nm) and Al_2O_3 (10 nm and 200 nm) particles as summarized in Table 2.

6.1 CONTRIBUTIONS

The following contributions to the understanding of adsorption at the liquid-solid interface required for advancements in the engineering of HTFs with enhanced thermal capacity have been made in this thesis:

1. The particle size was isolated as a crucial design parameter for nanofluids that utilize the effect of adsorption at the particle interface. Initial modeling efforts predicted that when particle mass fractions were low enough to prevent significant agglomeration (1-2%), nanoparticles on the order of 10 nm were necessary to detect a noticeable impact from the adsorbed layer. This criteria was confirmed experimentally in $LiNO_3$ fluids with Al_2O_3 nanoparticles. The experiments that used 10 nm Al_2O_3 particles resulted in anomalous changes to the enthalpy of fusion and heat capacity of $LiNO_3$, attributed to adsorption at the nanoparticle surface. In the trials with 200 nm Al_2O_3, no significant deviations from

pure was $LiNO_3$ observed. This indicates that particles on the order of 10 nm are indeed crucial for significant adsorption effects in nanofluids with low fractions of nanoparticles.

2. A procedure for experimentally determining the enthalpy of fusion and heat capacity of molten salt nanofluids using DSC was designed and verified. A sample preparation procedure for molten salt nanofluids was designed that disperses the particles at room temperature in an aqueous solution before evaporating the water without leaving any artifacts of the preparation steps. Detailed in Chapter 5, the preparation can be applied to any molten salt and particle combination. TGA was used to confirm that no residual water is left in the sample and that decomposition does not occur during the procedure as long as the appropriate temperatures are selected. Additionally, the intricacies involved with measuring molten salt samples in a DSC were elucidated. Issues associated with the low viscosity of the liquid phase of the salts can be avoided if correct sample pans are chosen and the samples are carefully prepared.

3. The experimental evidence in this thesis strongly suggests that the thermal behavior of an adsorbed layer at the liquid-solid interface will desorb at a single temperature rather than over a broad temperature range as some reports suggest [3], [29], [46]. This behavior is described in the second scenario of Chapter 2. Before the desorption temperature, the enthalpy of fusion and the heat capacity of the nanofluid will decrease as the adsorbed layer detracts from the mass of the bulk liquid as seen in the experimental results for Hitec HTS and $LiNO_3$, provided that the fluid-particle attraction is sufficiently strong. In order for the nanofluid to exhibit an enhanced thermal capacity, the desorption temperature must be within the useful operating temperature range of the end application and, more importantly, the desorption temperature must occur before the fluid decomposes.

4. The thickness of the adsorbed layer at the liquid-solid interface for a complex adsorbate was approximated using experimental data. Previous studies have demonstrated the thickness of this layer in monatomic fluids using MD simulations and TEM imaging [13], [37], but it has never (to the knowledge of the author) been accomplished using thermal measurement techniques and for adsorbates more complex than simple monatomic fluids.

The results suggest that the adsorbed layer thickness is 5.3-7.1 nm for $LiNO_3$ adsorbed to Al_2O_3, a very reasonable value when compared to literature results.

6.2 RECOMMENDATIONS FOR FUTURE WORK

There are several opportunities for future work in this area as the adsorption mechanism is not yet completely understood and very few practical implementations of systems that utilize liquid-solid adsorption have been attempted.

6.2.1 High Temperature Differential Scanning Calorimetry

The first facet that requires more attention is DSC measurements at higher temperatures. While many of the experiments in this study were limited by the maximum operating temperature of the DSC, as seen in Chapter 4, there are DSCs that operate at temperatures up to 1000°C. Caution must be exercised to avoid temperatures that are high enough to decompose the samples as the decomposition of molten salts can be violent and will certainly contaminate the DSC furnace. Given a fluid that remains stable at high temperatures, it is very possible that the desorption peak will be able to be measured in a nanofluid mixture, a large feat for the utility of these nanofluids in practical heat transfer systems. While it is unclear whether the desorption temperature of $LiNO_3$ on Al_2O_3 will occur before the $LiNO_3$ begins to decompose at 500°C, high temperature molten salts are a popular area of research and may yield more suitable candidates for desorption studies.

6.2.2 Isolate Influence of Particle Chemistry

Another logical step in advancing the understanding of the adsorption mechanism is to perform DSC experiments where the sole variable is the composition of the particle. Measuring the heat capacity and enthalpy of fusion of $LiNO_3$ nanofluids with similar sized particles of SiO_2, Al_2O_3, C, SiC, and Ag will clarify the role of the particle's chemistry on the strength of the adsorption energy and thus the thickness of the adsorbed layer. An analysis very similar to that of Chapter 5 will be useful.

DSC experiments of LiNO$_3$ with 1% 10 nm SiO$_2$ were performed and yielded preliminary results displayed in Figure 34. While complications with proper DSC calibration prevented reliable heat capacity measurements, enthalpy of fusion measurements were extremely repeatable with a standard deviation of 0.8% between multiple trials of the same sample and 1% deviation from the literature values for pure LiNO$_3$. The average of 3 SiO$_2$ nanofluid trials demonstrated a 4.9% decrease in enthalpy of fusion compared to pure LiNO$_3$ that results in a 3.9% mass fraction of adsorbed LiNO$_3$, γ. The adsorbed mass fraction is less than half the value for the same mass fraction of 10 nm Al$_2$O$_3$ particles suggesting a weaker interaction between LiNO$_3$ and SiO$_2$ than between LiNO$_3$ and Al$_2$O$_3$. While the consistency of the enthalpy of fusion data allowed for a 4.9% change to be measured with confidence, a similar change in heat capacity is difficult to accurately resolve in the DSC. Furthermore, the change in heat capacity from pure LiNO$_3$ is expected to be less than the 4.9% change in enthalpy of fusion as discussed in Section 5.2. For this reason, future experiments should focus on a higher particle mass fraction that allows for a larger quantity of adsorbed LiNO$_3$ while avoiding significant agglomeration of the particles.

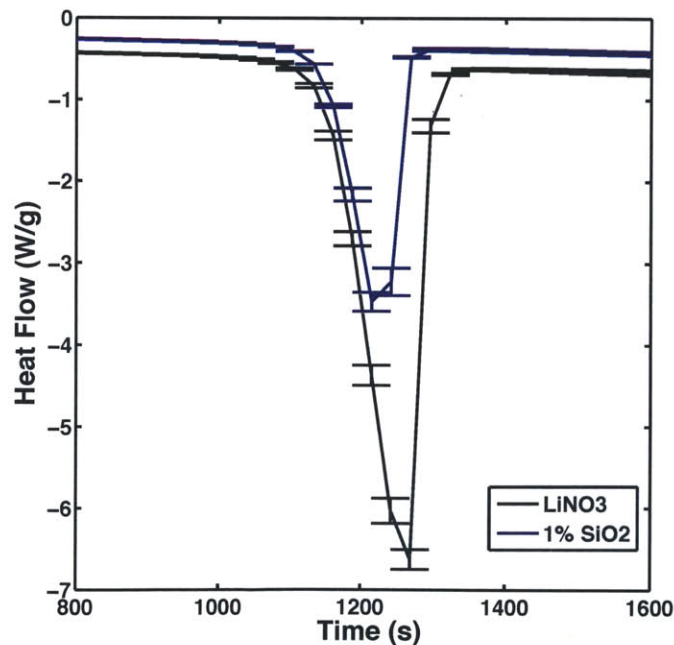Figure 34. Heat flow values from DSC data for LiNO$_3$ and LiNO$_3$ with 1% 10 nm SiO$_2$. The integral of each curve is the enthalpy of fusion for each fluid. Error bars represent one standard deviation from the average value of multiple trials.

78

Further studies are required to capture the effect of various ~10 nm nanoparticles on both enthalpy of fusion and heat capacity. The analysis presented in this thesis can be used to quantify the mass of adsorbed liquid and determine which particle chemistry demonstrates the largest adsorption effect and thus the most potential for enhanced thermal capacity.

6.2.3   Environmental Transmission Electron Microscopy

Finally, the understanding of adsorption in nanoparticle mixtures would greatly benefit from TEM images of the fluid. The images can be used to verify the existence and thickness of the adsorbed layer on the surface of the particles as has been demonstrated in the literature for a simple liquid-solid interface [37]. Additionally, the relative agglomeration of the particles can be quantified using TEM images. These TEM images were initially planned for inclusion in this thesis, but the following complications proved to make the imaging prohibitively difficult given the timeframe of the project.

In order for the TEM images to provide an insightful view of the nanofluid behavior, the nanoparticle mixture must be imaged in a liquid phase. While a hot stage can be used to raise the mixture past its melting temperature inside the TEM, the ultrahigh vacuum of the TEM will quickly evaporate the sample. The literature reports of TEM images at the liquid-solid interface were only possible because aluminum was used as the fluid [37]. The vapor pressure of liquid aluminum is sufficiently low ($5*10^{-6}$ Pa) that it remains liquid within the ultrahigh vacuum of the TEM (10^{-5} Pa). Since the vapor pressure of liquid $LiNO_3$ is $5*10^{-4}$ Pa, it will not survive in the TEM environment. The remedy to this issue can be rather complicated. An environmental chamber must be microfabricated for use within the TEM to protect the liquid sample from the ultrahigh vacuum pressure [52]. The chamber includes electron-transparent windows, often made of SiN, that are capable of containing the liquid while allowing electrons to pass through the sample to the TEM's detector with a small reduction in quality. While this has been successfully demonstrated in literature, additional engineering of the chamber would be required to accommodate a sample that is solid at room temperature and must be heated within the TEM. While this experiment would be very difficult, the in situ images of nanofluid behavior and liquid-solid adsorption would be incredibly valuable.

Chapter 7

7. Appendix

The following steps detail the procedure for preparing salt and nanoparticle mixtures. This procedure is applicable to most molten salts with a melting point below the maximum temperature of a hot plate, typically 500°C, and a low concentration of solid particles, <10% by mass.

1. Measure 50 mL deionized water in a clean glass jar with a sealable lid.

2. Add 10 g salt to the glass jar. Eutectic mixtures will require multiple constituents with a total mass of 10 g.

3. Add the appropriate quantity of nanoparticles to the jar for the desired particle mass fraction. This should be done in a proper enclosure for handling nanoparticles.

4. Place the sealed jar in an ultrasonicator for 2 hours.

5. Dispense 30 mL solution into a beaker or flask. A flask with a glass hose connector is ideal (Figure 22). Place the flask on a hot plate at 90°C in a fume hood overnight or until the water has evaporated from the solution.

6. Connect a nitrogen supply to the flask and ensure proper circulation of nitrogen within the flask as seen in Figure 23. Place the flask on a hot plate at a temperature above the melting temperature of the fluid and below the decomposition temperature, typically 400°C. Purge the flask with nitrogen and allow nitrogen to flow through the flask while the hot plate remains on for 1 hour. Continue to purge the flask with nitrogen once the hot plate has been turned off and the salt is solidifying. Swirling the salt as it cools will help disperse the nanoparticles.

7. Place flask in a vacuum oven set to 150°C and 3 kPa vacuum pressure overnight. Allow the mixture to cool in the oven before removing the vacuum pressure.

8. At this point, some salts are very sensitive to humidity in the air and require storage in an airtight container. This is one of the most important steps in the procedure. Exposure to the atmosphere should be limited when possible. Samples that are exposed to the atmosphere (in a DSC pan or similar sample holder) should be tested immediately and discarded after several hours.

7.2 METTLER TOLDEO DIFFERENTIAL SCANNING CALORIMETER STANDARD OPERATING PROCEDURE

7.2.1 Sample Preparation

- If the procedure will exceed 100°C, pierce the aluminum lid with the included needle
- Record the weight of the empty 40 µL aluminum pan and lid in grams and zero the scale
- Fill the pan with the sample (25 µL usually works best for liquid samples)
- Seal the lid to the pan using Mettler Toledo pan press
- Record the weight of the filled pan in grams
  - o This will be the weight of the sample only
- Using the included tool, gently press the lid of the pan inwards, towards the sample, to minimize space between the base of the pan and the lid

7.2.2 Running Experiments with the STARe Software

- Ensure that the DSC, chiller, and nitrogen tank are connected properly and turned on
  - o On/Off switch for the DSC is on the back of the machine
- Place the pan in an empty pan holder position on the DSC
- Record the required information in the Polymer_DSC.txt file on the desktop
- Launch the STARe software (username: METTLER, no password)
- In the DSC (METTLER) window, choose Routine Editor in the left pane
- Choose Open... and select desired method or create your own. First, run the experiment on the blank pan by checking the Run Blank Curve box, setting the weight to 0 mg, setting the position to an empty pan, and selecting Send Experiment
- Add your other experiments to the queue using a similar process
  - o The Weight field refers only to the weight of the sample (not the pan)
  - o If heat capacity is being measured, run the same method on one of the sapphire samples loaded in the pan holder
- Add the Shutdown Iso 25C 15 min method to the end of the experiment queue with a sample weight of 0 and position set to an empty pan
  - o This prevents the DSC from idling at an extreme temperature after the last method is run
- Once Experiments are completed, the chiller, nitrogen tank, and DSC can be turned off (switch in the back) and the computer can be shut down

7.2.3 Analyzing Data for Specific Heat Capacity

- Once experiments are completed, choose Session > Evaluation Window from the METTLER: STARe Default DB window
- In the evaluation window, choose File > Open Curve... and select your experiment as well as the sapphire method that was run
- While holding Control, first select the sample curve and then select the sapphire curve. Both will turn pink when selected.

- Choose DSC > Cp by sapphire... from the menu and press OK, leaving the molar mass as 0
  - If you receive an error, choose TA > Curve vs. Time from the evaluation window
- The blue curve represents the specific heat of the sample
- This data can be exported as a .txt file by choosing File > Import/Export > Export Other Format...

7.2.4   Analyzing Data for Enthalpy of Fusion

- Once experiments are completed, choose Session > Evaluation Window from the METTLER: STARe Default DB window
- In the evaluation window, choose File > Open Curve... and select your experiment
- Select the sample curve. It will turn pink when selected
- Choose TA > Normalize Data by Weight and select the new curve
- Choose Math > Integration and use the lower arrow on each side of the integral line to choose the appropriate area
  - If you receive an error, choose TA > Curve vs. Time from the evaluation window
- The enthalpy of fusion will be displayed in the Integral field of the floating text

7.3   MATLAB CODE FOR MODIFIED MIXING RULE MODEL

```
%Matt Thoms
%Model for proposed melting layer around nanoparticles in LiNO3

clear, clc

%Calculating increase in Cp as a function of particle diameter

htotal = 355; %Enthalpy of LiNO3, J/g

%Assumptions & Variables

densnano = 3.97e6; %g/m^3
densliq = 1.781e6;
densmelt = 2.38e6;


cpnano = 112.55/101.96; %CRC values at 600K
cpliq = 2;


delT = 50;


percwtnano = 0.01;
percvolnano = (densliq/densnano)*percwtnano;


%Nanoparticle dimensions
dnano = [1e-9:.1e-10:15e-9];
rnano = dnano./2;


tmelt1 = [1e-9];
tmelt2 = [2e-9];
tmelt5 = [5e-9];
tmelt10 = [10e-9];


rmelt1 = rnano+tmelt1;
rmelt2 = rnano+tmelt2;
rmelt5 = rnano+tmelt5;
rmelt10 = rnano+tmelt10;



percvolmelt1 = (percvolnano.*((rmelt1.^3)+(rnano.^3)))./(rnano.^3);
percvolmelt2 = (percvolnano.*((rmelt2.^3)+(rnano.^3)))./(rnano.^3);
percvolmelt5 = (percvolnano.*((rmelt5.^3)+(rnano.^3)))./(rnano.^3);
percvolmelt10 = (percvolnano.*((rmelt10.^3)+(rnano.^3)))./(rnano.^3);

%Begin calculations

cpeffn1 = (percvolnano*densnano*cpnano)+((1-percvolnano-
percvolmelt1).*densliq.*cpliq)+(percvolmelt1.*densmelt.*htotal./delT);
cpeffd1 = (percvolnano*densnano)+((1-percvolnano-
percvolmelt1).*densliq)+(percvolmelt1.*densmelt);
cpeff1 = cpeffn1./cpeffd1;

cpeffn2 = (percvolnano*densnano*cpnano)+((1-percvolnano-
percvolmelt2).*densliq.*cpliq)+(percvolmelt2.*densmelt.*htotal./delT);
```

```
cpeffd2 = (percvolnano*densnano)+((1-percvolnano-
percvolmelt2).*densliq)+(percvolmelt2.*densmelt);
cpeff2 = cpeffn2./cpeffd2;

cpeffn5 = (percvolnano*densnano*cpnano)+((1-percvolnano-
percvolmelt5).*densliq.*cpliq)+(percvolmelt5.*densmelt.*htotal./delT);
cpeffd5 = (percvolnano*densnano)+((1-percvolnano-
percvolmelt5).*densliq)+(percvolmelt5.*densmelt);
cpeff5 = cpeffn5./cpeffd5;

cpeffn10 = (percvolnano*densnano*cpnano)+((1-percvolnano-
percvolmelt10).*densliq.*cpliq)+(percvolmelt10.*densmelt.*htotal./delT);
cpeffd10 = (percvolnano*densnano)+((1-percvolnano-
percvolmelt10).*densliq)+(percvolmelt10.*densmelt);
cpeff10 = cpeffn10./cpeffd10;


%Plot
dnanoplot = dnano.*(1e9);
cpincrease1 = ((cpeff1./cpliq)-1).*100;
cpincrease2 = ((cpeff2./cpliq)-1).*100;
cpincrease5 = ((cpeff5./cpliq)-1).*100;
cpincrease10 = ((cpeff10./cpliq)-1).*100;


figure;
hold on
plot(dnanoplot, cpincrease1, 'b', 'LineWidth', 2)
plot(dnanoplot, cpincrease2, 'r', 'LineWidth', 2)
plot(dnanoplot, cpincrease5, 'g', 'LineWidth', 2)
plot(dnanoplot, cpincrease10, 'k', 'LineWidth', 2)


set(gca,'Linewidth',2,'fontsize',12,'fontweight','bold')
xlabel('Nanoparticle Diameter (nm)');
ylabel('Percent Increase in Heat Capacity');
h = legend('1 nm', '2 nm', '5 nm', '10 nm');

v = get(h,'title');
set(v,'string','Adsorbed Layer Thickness');

%title('Nanoparticle Model');
hold off
```

8. Bibliography

[1]   J. Buongiorno, "Convective transport in nanofluids," *Journal of Heat Transfer*, vol. 128, p. 240, 2006.

[2]   F. Vanek and L. Albright, *Energy Systems Engineering*. McGraw Hill, 2008.

[3]   D. Shin and D. Banerjee, "Effects of silica nanoparticles on enhancing the specific heat capacity of carbonate salt eutectic (work in progress)," *The International Journal of Structural Changes in Solids*, vol. 2, no. 2, pp. 25–31, Jun. 2011.

[4]   P. A. R. T. C. W. team, Ed., *Climate Change 2007: Synthesis Report*. Intergovernmental panel on climate change, WMO and UNEP, 2008.

[5]   L. Xue, P. Keblinski, S. Phillpot, S. Choi, and J. Eastman, "Effect of liquid layering at the liquid-solid interface on thermal transport," *International Journal of Heat and Mass Transfer*, vol. 47, no. 19, pp. 4277–4284, 2004.

[6]   "The World Factbook," *Central Intelligence Agency*, 21-Jan.-2012. [Online]. Available: http://www.cia.gov. [Accessed: 21-Mar.-2012].

[7]   "U.S. Energy Consumption by Energy Source," *U.S. Energy Information Administration*, 21-Mar.-2008. [Online]. Available: http://www.eia.gov. [Accessed: 21-Mar.-2012].

[8]   Sargent & Lundy LLC Consulting Group, "Executive Summary: Assessment of Parabolic Trough and Power Tower Solar Technology Cost and Performance Forecasts," pp. 1–47, Oct. 2003.

[9]   B. Kelly, "Nexant Parabolic Trough Solar Power Plant Systems Analysis," pp. 1–59, Jul. 2006.

[10]   U.S. Department of Energy.

[11]   L. Moens, D. Blake, D. Rudnicki, and M. Hale, "Advanced thermal storage fluids for solar parabolic trough systems," *J Sol Energ-T Asme*, vol. 125, no. 1, pp. 112–116, 2003.

[12]   B. Wu, R. Reddy, and R. Rogers, "Novel ionic liquid thermal storage for solar thermal electric power systems," *SOLAR ENGINEERING*, 2001.

[13]   W. D. Kaplan and Y. Kauffmann, "Structural Order in Liquids Induced by Interfaces with Crystals," *Annu. Rev. Mater. Res.*, vol. 36, no. 1, pp. 1–48, Aug. 2006.

[14]   R. Radhakrishnan, K. Gubbins, and M. Sliwinska-Bartkowiak, "Effect of the fluid-wall interaction on freezing of confined fluids: Toward the development of a global phase diagram," *J. Chem. Phys.*, vol. 112, p. 11048, 2000.

[15]   D. B. Donghyun Shin, "Experimental Investigation of Molten Salt Nanofluid for Solar Thermal Energy Application," *Proceedings of the ASME/JSME 2011 8th Thermal Engineering Joint Conference*, pp. 1–6, Dec. 2011.

[16]   M. Eck and K. Hennecke, "Heat Transfer Fluids for Future Parabolic Trough Solar Thermal Power Plants," *Proceedings of ISES World Congress 2007 (Vol. I–Vol. V)*, pp. 1806–1812, 2009.

[17]   Y. Liu, G. Wu, H. Fu, Z. Jiang, S. Chen, and M. Sha, "Immobilization and melting point depression of imidazolium ionic liquids on the surface of nano-SiOx particles," *Dalton Trans.*, vol. 39, no. 13, p. 3190, 2010.

[18] T. Humplik, "Investigating the Adsorption and Transport of Water in MFI Zeolite Pores for Water Desalination," pp. 1–74, Aug. 2010.

[19] Y. Zhang, X. Hu, and X. Wang, "Theoretical analysis of convective heat transfer enhancement of microencapsulated phase change material slurries," *HEAT AND MASS TRANSFER*, vol. 40, no. 1, pp. 59–66, Dec. 2003.

[20] R. Bradshaw and N. Siegel, "Molten nitrate salt development for thermal energy storage in parabolic trough solar power systems," *Proceedings of ES2008, Energy Sustainability*, pp. 10–14, 2008.

[21] K. Xing, Y. Tao, and Y. Hao, "Performance evaluation of liquid flow with PCM particles in microchannels," *Journal of Heat Transfer*, vol. 127, p. 931, 2005.

[22] A. S. F. T. A. Materials, "Enthalpies of Fusion and Crystallization by Differential Scanning Calorimetry," ASTM International, West Conshohocken, PA, 2008.

[23] Y. Fang, S. Kuang, X. Gao, and Z. Zhang, "Preparation of nanoencapsulated phase change material as latent functionally thermal fluid," *Journal of Physics D: ...*, 2009.

[24] A. S. F. T. A. Materials, *Standard test method for determining specific heat capacity by differential scanning calorimetry*. 2005, p. 6.

[25] S. Kuravi, K. Kota, J. Du, and L. Chow, "Numerical Investigation of Flow and Heat Transfer Performance of Nano-Encapsulated Phase Change Material Slurry in Microchannels," *Journal of Heat Transfer*, vol. 131, p. 062901, 2009.

[26] Y. Hong, S. Ding, W. Wu, J. Hu, A. A. Voevodin, L. Gschwender, E. Snyder, L. Chow, and M. Su, "Enhancing Heat Capacity of Colloidal Suspension Using Nanoscale Encapsulated Phase-Change Materials for Heat Transfer," *ACS Appl. Mater. Interfaces*, vol. 2, no. 6, pp. 1685–1691, Jun. 2010.

[27] M. Kenisarin, "High-temperature phase change materials for thermal energy storage," *Renewable and Sustainable Energy Reviews*, vol. 14, no. 3, pp. 955–970, 2010.

[28] D. Shin, B. Jo, H.-E. Kwak, and D. Banerjee, "Investigation of High Temperature Nanofluids for Solar Thermal Power Conversion and Storage Applications," *Proceedings of the International Heat Transfer Conference*, pp. 1–9, Feb. 2010.

[29] D. Shin and D. Banerjee, "Enhancement of specific heat capacity of high-temperature silica-nanofluids synthesized in alkali chloride salt eutectics for solar thermal-energy storage applications," *International Journal of Heat and Mass Transfer*, vol. 54, no. 5, pp. 1064–1070, Feb. 2011.

[30] N. Araki, M. Matsuura, A. Makino, T. Hirata, and Y. Kato, "Measurement of thermophysical properties of molten salts: Mixtures of alkaline carbonate salts," *International Journal of Thermophysics*, vol. 9, no. 6, pp. 1071–1080, 1988.

[31] D. B. Byeongnam Jo, "Enhanced Specific Heat Capacity of Molten Salts Using Organic Nanoparticles," pp. 1–8, Aug. 2011.

[32] D. Shin and D. Banerjee, "Enhanced Specific Heat of Silica Nanofluid," pp. 1–15, Jul. 2010.

[33] J. N. Israelachvili, *Intermolecular and Surface Forces, Third Edition: Revised Third Edition*, 3rd ed. Academic Press, 2011, p. 704.

[34] W. Curtin, "Density-functional theory of the solid-liquid interface.," *Phys. Rev. Lett.*, vol. 59, no. 11, pp. 1228–1231, Sep. 1987.

[35] S. H. Garofalini and W. Luo, "Molecular Dynamics Simulations of Calcium Silicate Intergranular Films between Silicon Nitride Crystals," *J Am Ceram Soc*, vol. 86, no. 10, pp. 1741–1752, Oct. 2003.

[36]   S. Blonski and S. Garofalini, "Atomistic structure of calcium silicate intergranular films in alumina studied by molecular dynamics simulations," *J Am Ceram Soc*, vol. 80, no. 8, pp. 1997–2004, 1997.

[37]   Y. Kauffmann, S. H. Oh, C. T. Koch, A. Hashibon, C. Scheu, M. Rühle, and W. D. Kaplan, "Quantitative analysis of layering and in-plane structural ordering at an alumina-aluminum solid-liquid interface," *ACTA MATERIALIA*, pp. 1–9, Apr. 2011.

[38]   C. Gerardi, D. Cory, J. Buongiorno, L.-W. Hu, and T. Mckrell, "Nuclear magnetic resonance-based study of ordered layering on the surface of alumina nanoparticles in water," *Appl. Phys. Lett.*, vol. 95, no. 25, p. 253104, 2009.

[39]   M. Miyahara and K. Gubbins, "Freezing/melting phenomena for Lennard-Jones methane in slit pores: A Monte Carlo study," *J. Chem. Phys.*, vol. 106, no. 7, pp. 2865–2880, 1997.

[40]   M. Sliwinska-Bartkowiak, J. Gras, R. Sikorski, R. Radhakrishnan, L. Gelb, and K. Gubbins, "Phase transitions in pores: experimental and simulation studies of melting and freezing," *Langmuir*, vol. 15, no. 18, pp. 6060–6069, 1999.

[41]   B. Coasne, J. Czwartos, M. Sliwinska-Bartkowiak, and K. E. Gubbins, "Freezing of mixtures confined in silica nanopores: Experiment and molecular simulation," *J. Chem. Phys.*, vol. 133, no. 8, p. 084701, 2010.

[42]   M. Zhang, M. Efremov, F. Schiettekatte, E. Olson, A. Kwan, S. Lai, T. Wisleder, J. Greene, and L. Allen, "Size-dependent melting point depression of nanostructures: Nanocalorimetric measurements," *Phys. Rev. B*, vol. 62, no. 15, pp. 10548–10557, 2000.

[43]   P. Keblinski, R. Prasher, and J. Eapen, "Thermal conductance of nanofluids: is the controversy over?," *J Nanopart Res*, vol. 10, no. 7, pp. 1089–1097, 2008.

[44]   P. Keblinski, S. Phillpot, S. Choi, and J. Eastman, "Mechanisms of heat flow in suspensions of nano-sized particles (nanofluids)," *International Journal of Heat and Mass Transfer*, vol. 45, no. 4, pp. 855–863, 2002.

[45]   M. Maeso and J. Largo, "The heat capacities of LiNO3 and CsNO3 from 350 to 700 K," *Thermochimica Acta*, vol. 222, no. 2, pp. 195–201, 1993.

[46]   D. Shin and D. Banerjee, "Enhanced Specific Heat of Silica Nanofluid," *Journal of Heat Transfer*, vol. 133, no. 2, p. 024501, 2011.

[47]   L. Thomas, "Making Accurate DSC and MDSC Specific Heat Capacity Measurements with the Q1000 Tzero DSC," pp. 1–9, May 2003.

[48]   Y. Takahashi and R. Sakamoto, "Heat capacities and latent heats of LiNO/sub 3/, NaNO/sub 3/, and KNO/sub 3," *Int. J. Thermophys.;(United ...*, 1988.

[49]   K. Stern, *High Temperature Properties and Thermal Decomposition of Inorganic Salts With Oxyanions*. CRC Press, 2001.

[50]   D. Lide, *CRC Handbook of Chemistry and Physics*. 2011.

[51]   S. Oh, Y. Kauffmann, C. Scheu, W. Kaplan, and M. Ruhle, "Ordered liquid aluminum at the interface with sapphire," *Science*, vol. 310, no. 5748, p. 661, 2005.

[52]   N. de Jonge and F. M. Ross, "Electron microscopy of specimens in liquid," *Nature Nanotechnology*, vol. 6, no. 11, pp. 695–704, Oct. 2011.